Stratigraphic record of an extreme hydro-sedimentary event in steep mountainous environments: a case study in the Roya Valley

Raphaël Kerverdo, S Lafuerza, C. Gorini, E. Fouache, Didier Granjeon, Rémy Deschamps, Sébastien Migeon, J.L. Rubino, Pierre-Yves Lagrée, M Jafari, et al.

Catena 269 (2026) 110054

Contents lists available at ScienceDirect

Catena

journal homepage: www.elsevier.com/locate/catena

Stratigraphic record of an extreme hydro-sedimentary event in steep mountainous environments: a case study in the Roya Valley

Raphaël Kerverdo [a,*], S. Lafuerza [a], C. Gorini [a], E. Fouache [b], D. Granjeon [c], R. Deschamps [c], S. Migeon [d,a], J.L. Rubino [a], P.Y. Lagrée [e], M. Jafari [e], N. Bianchi [f]

[a] Institut des Sciences de la Terre de Paris (ISTeP), Sorbonne Université, CNRS-INSU, 75005 Paris, France
[b] Laboratoire Médiations, Institut de Géographie, Sorbonne Université, Paris, France
[c] IFP Energies Nouvelles, Rueil-Malmaison, France
[d] Université Côte d'Azur, CNRS, Observatoire de la Côte d'Azur, IRD, Géoazur, 250 rue Albert Einstein, 06560 Valbonne, France
[e] Institut Jean le Rond d'Alembert, Sorbonne Université, Paris, France
[f] Musée départemental des Merveilles, Tende, France

ARTICLE INFO

Keywords:
Extreme flood
Deposits
Debris flow
Debris flood
Hyperconcentrated flow
Stratigraphic record

ABSTRACT

This study investigates the sedimentary deposits produced by Storm Alex (2 October 2020) in the Roya Valley (southeastern France), focusing on three sub-valleys (Dente, Consciente, and Cairos) to better understand the flow processes and their associated lithofacies. Lithology and morphometric parameters played an important role in controlling flow behaviour and sediment availability. In the Dente torrent, the remobilisation of glacial and colluvial deposits triggered debris flows that evolved into hyperconcentrated and bedload flows, forming sheetflood deposits on the Vievola fan. In contrast, the Consciente torrent was dominated by bedload and hyperconcentrated flows with a strong sandy component, derived from the erosion of migmatitic formations of the Argentera-Mercantour massif, while debris flows were locally linked to landslide inputs. The Cairos River, characterised by gentler slopes and a wider valley floor incised into Wurmian terraces, was dominated by bedload processes, with localised debris flows from right-bank tributaries (from marly-limestones) enhancing sediment cascades and channel widening. A significant difference (~5 wt%) in fine-grained content (clay + silt) was identified between debris flows in the Dente torrent and bedload/hyperconcentrated deposits in the Consciente and Cairos catchments, indicating distinct transport and depositional dynamics. In addition, slope breaks were key locations for the end-members of debris flows such as major channel widenings (width ratio > 3) favored their deposition. This case study highlights the complexity of flow transitions (from debris flows to bedload transport) and emphasises the role of lithological and topographic constraints in controlling sedimentary dynamics during extreme events. The findings emphasise the value of interdisciplinary, multi-scale approaches in documenting and understanding extreme hydro-sedimentary events in mountainous regions.

1. Introduction

In recent decades, post-flood studies in mountain environments have primarily focused on identifying the controlling factors of active-channel widening (Liébault et al., 2024; Rinaldi et al., 2016; Scorpio et al., 2018, 2022; Surian et al., 2016) and the mobilisation of large wood (Comiti et al., 2016; Martini et al., 2025; Piton et al., 2024; Ruiz-Villanueva et al., 2018) during large/extreme floods. These extreme floods whose discharge often exceeded the centennial return period are associated with intense rainfall over short durations and resulted in marked erosion and aggradation (Liébault et al., 2024; Rathburn et al., 2017; Steinritz et al., 2024). Main findings of these articles (Ruiz-Villanueva et al., 2023) highlighted the importance of the hydraulic variables (Magilligan, 1992; Sholtes et al., 2018; Yochum et al., 2017) but also of the morphometric parameters such as slope (Surian et al., 2016), width ratio (Krapesch et al., 2011), confinement index (Comiti et al., 2016b; Lucía et al., 2018), bed texture type (Rinaldi et al., 2016), net aggradation (Liébault et al., 2024) and large quantities of wood mobilised (Martini et al., 2025; Piton et al., 2024). To better characterise the erosion, transport, and deposition processes of extreme events, a variety of complementary approaches were developed and compiled by Morel et al. (2023): (1) empirical methods link deposit volumes to descriptive

* Corresponding author.
E-mail address: raphael.kerverdo@sorbonne-universite.fr (R. Kerverdo).

https://doi.org/10.1016/j.catena.2026.110054
Received 25 February 2025; Received in revised form 18 January 2026; Accepted 22 March 2026
Available online 17 April 2026

catchment parameters (e.g. Marchi and D'Agostino, 2004), (2) hydrological methods correlated mobilised volumes with water discharge (Rickenmann and Koschni, 2010), (3) geomorphological methods identified sediment sources along the channel network (Hungr et al., 1984; Jakob, 2021) and (4) historical analyses used archival data to reconstruct past event intensity and frequency (Hugerot et al., 2024). However, post-event analyses have seldom addressed the types of deposits left by these floods (Brenna et al., 2020). Indeed, Brenna et al. (2023) demonstrated the role of intense bedload transport (debris flood) as a factor controlling channel widening during Vaïa Storm. But impact of the flow processes during large floods remains poorly studied as depicted by Brenna et al. (2020).

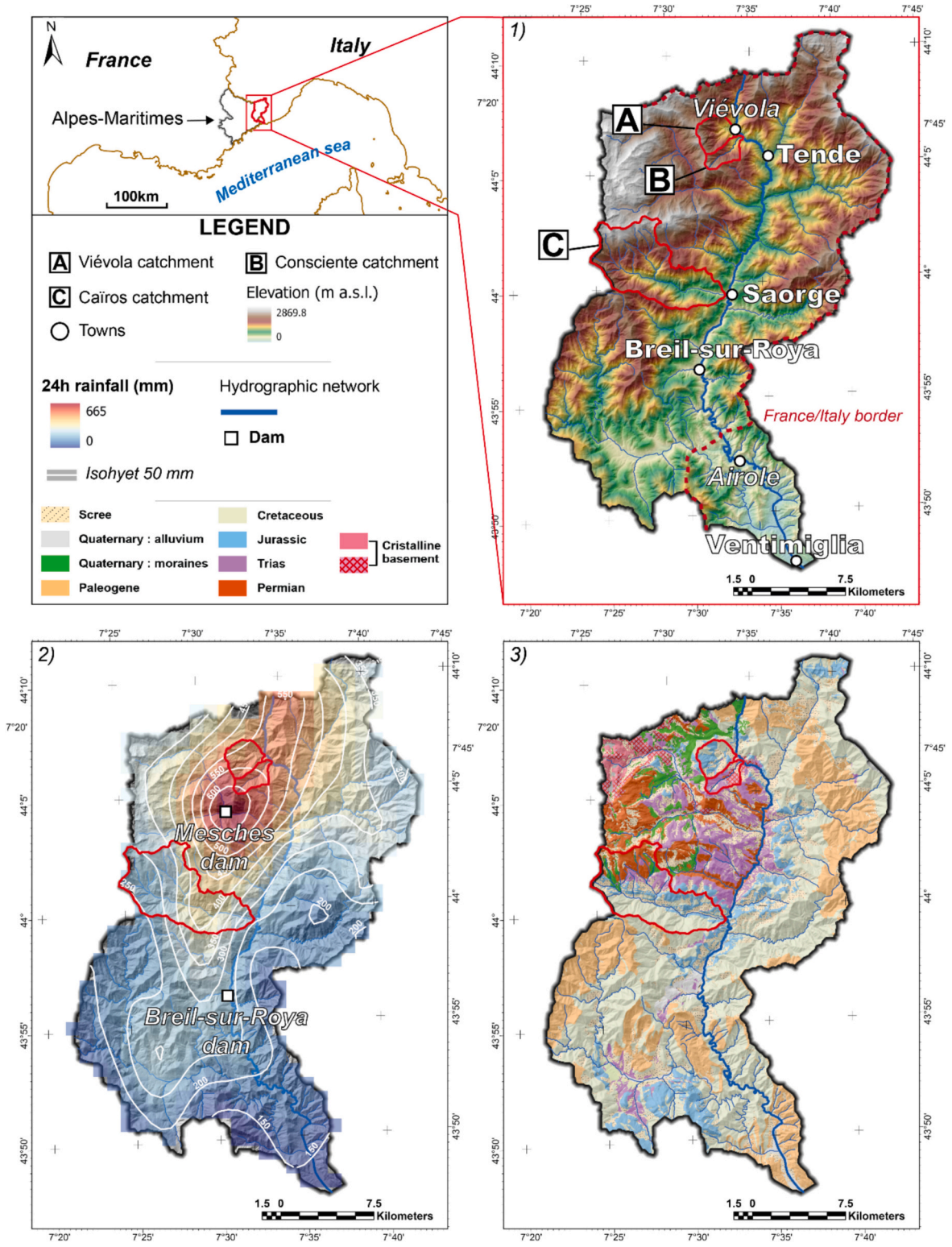

Fig. 1. 1) Elevation map of the Roya catchment. France/Italy border is shown with a red dotted polyline. (A) Vievola catchment, (B) Consciente catchment, and (C) Cairos catchment. 2) 24-hour rainfall map of Storm Alex based on Météo France covering the period from 02/10/2020 06:00 UTC to 03/10/2020 06:00 UTC. 3) Geological map, compiled from the BRGM 1:50,000 geological map (Gèze and Nesteroff, 1996) and data from Regione Liguria (https://www.regione.liguria.it/).

The aim of this study is to complement the dynamics of the flow processes occurring in different catchment basins of the same valley affected by an extreme event. This is coupled with a morphometric analysis of indices such as changes in channel width, slope and the role of lithology in the flow generation. What flood parameters can be inferred and what flood dynamics reconstructed from a sedimentary analysis of flood deposits?

Sediment transfer in mountainous environments can occur through various types of flow processes:

Debris flows (Cruden and Varnes, 1996; Hungr et al., 2014; Lowe, 1982) are gravity-driven mass movements occurring on steep slopes. They exhibit non-Newtonian rheology with viscoplastic properties (Costa, 1984; Iverson, 1997; Middleton and Hampton, 1973) and are characterised by high sediment concentrations (typically 60–80% by volume) and rapid propagation velocities, ranging from a few to several tens of metres per second (Costa, 1984; Hungr et al., 2014; Iverson, 1997). Their high erosive capacity can lead to severe destruction of infrastructures and landscapes (Costa, 1984). Debris flows are typically plug flow.

The term “debris flood” is relatively recent (Hungr et al., 2001). It describes a type of intense bedload transport (Carling, 1987) in which the coarse particles of the channel bed become fully mobilised and move as a turbulent mass flow (Church and Jakob, 2020; Manville and White, 2003). All particles are transported as bedload over distances of several hundred metres (Church and Jakob, 2020). These flows are entirely turbulent and typically occur in steep, confined channels.

The concept of hyperconcentrated flow has been used inconsistently in the literature, as pointed out by several authors (Brenna et al., 2020; Church and Jakob, 2020; Manville and White, 2003). In its classical sense, it refers to a suspension-dominated flow containing at least 20% sediment by volume (Pierson, 2005a, 2005b), and is commonly associated with volcanic mudflows, or “lahars” (Cronin et al., 1999; Smith, 1986; Thouret et al., 2020). The rheological behaviour of a hyperconcentrated flow can be assimilated to a plastic, non-Newtonian fluid, evolving between turbulent and laminar regimes (Coussot and Meunier, 1996; Pierson and Costa, 1987). Here, we adopt the terminological refinement proposed by Brenna et al. (2020) defining hyperconcentrated flows as a flow dominated by a high suspended-sediment load. These flows may, in some cases, occur concomitantly with debris floods (Brenna et al., 2020; Church and Jakob, 2020).

Finally, water flows (Pierson and Costa, 1987) correspond to Newtonian, fully turbulent flows characterised by very low sediment concentrations (Walling and Webb, 1996). Particle motion occurs through a combination of suspension and bedload transport (Carling, 1987; Pierson and Costa, 1987), driven by the combined action of gravity and hydraulic forces exerted by the flowing water on individual particles.

The high valleys of the Tinée, Vésubie, and Roya rivers (Alpes-Maritimes, southeastern France) were severely impacted by Storm Alex from which occurred between midday on 2 October 2020, to the early morning of 3 October 2020 (Fig. 1). This extreme event resulted from the rapid intensification of a low-pressure system over the Atlantic Ocean. Storm Alex made landfall on the west coast of France during the night of October 1st, generating a strong northerly influx of warm, humid air from the Mediterranean Sea. This configuration led to an exceptional rainfall event in the mountainous hinterland of Alpes-Maritimes. In the Roya Valley, maximum 24-h rainfall (Fig. 1) reached approximately 663 mm at the Mesches dam (Fig. 1), exceeding the 1000-year return period threshold (Carrega and Michelot, 2021; Cerema, 2021; ONF-RTM, ONF-DRN, INRAE-ETNA, 2023). These extreme conditions induced major morphological changes in catchments and river channels, as documented by Liébault et al. (2024) and Kerverdo et al. (2025) for the Vievola catchment. Although data were limited, the Airole gauging station (Italy) recorded a peak discharge of 1526 m^3/s (ARPAL – Liguria) consistent with hydrological models estimates between 1100 and 1800 m^3/s at Breil-sur-Roya (ONF-RTM, ONF-DRN, INRAE-ETNA, 2023; Pons et al., 2024). These values correspond to a flood return period exceeding 100 years, based on the 1926 flood reference, when peak discharge was estimated at 900 m^3/s (ONF-RTM, ONF-DRN, INRAE-ETNA, 2023). Following this catastrophic event, the region experienced a three-year drought, during which hydrological activity in the torrents was minimal. This unique post-flood context provided ideal conditions for documenting and interpreting the sedimentary imprint left by Storm Alex.

Hence, this study aims to comprehensively characterise deposits generated by extreme rainfall and flooding using the case of Storm Alex in the Roya River catchment. It seeks to clarify their spatial distribution in relation to the specific environmental conditions under which they form, thereby offering a more refined understanding of the mechanisms and impacts of such rare hydro-sedimentary events. The results provide valuable insights for better constraining erosion and deposition patterns in mountain river catchments and for improving flash-flood assessments in similar morphological and climatic settings.

2. Study area

The Roya Valley is a Franco-Italian valley located in southeastern France (Fig. 1). Its eastern and northern boundaries follow the international border between France and Italy. The upper and middle sections of the valley lie within French territory, while the lower section extends into Italian territory (Fig. 1-1).

2.1. Geological context of the Roya Valley

Situated at the southeastern edge of the Argentera-Mercantour massif, the Roya Valley displays a diverse geological setting (Fig. 1). In the northwest, the crystalline basement of the massif is mainly composed of granites and anatexites (Figs. 1–3) (Bigot-Cormier, 2002; Lanteaume, 1991; Sanchez et al., 2011). This basement is overlain by Permian pelites and quartzites, followed by Lower Triassic sandstones, which form prominent outcrops on the right bank of the Roya River (Barrier et al., 2009; Faure-Muret, 1955; Julian, 1980). Above these formations, Middle Triassic to Lower Jurassic, limestones and dolomites are present (Gèze and Nesteroff, 1996). The entire Permo-Triassic sequence is tectonically overlain by a Jurassic to Upper Cretaceous nappe (Figs. 1–3), which crops out mainly in southwestern and eastern parts of the valley. This is further overlain by clayey limestone and sandstones of Upper Eocene age (Figs. 1–3).

2.2. Selected torrential rivers

Three tributaries affected by Storm Alex were selected for this study (Fig. 1, Table 1): the Dente and Consciente torrents, and the Cairos River. The selection criteria include each tributary's activation during the storm, the volume of rainfall received (Figs. 1 and 2), the presence of preserved flood-related deposits, and accessibility for field investigations.

The Dente torrent is part of the Vievola's catchment (Fig. 2A). It lies on the right bank of the Roya River, where rainfall reached 547 mm in 24 h (Table 1). Covering only 2.4 km^2, it is the smallest of the selected catchments, with a channel length of 3 km (Table 1). Elevation ranges from 2281 m a.s.l to 1013 m a.s.l (Table 1), and the hillslopes are steep, with a mean gradient of 73% (Fig. 2A, Table 1). The Dente torrent is fed by a tributary called the Rabay torrent (Fig. 2A), both of which exhibit large gullies in their headwaters. Geologically, the Dente torrent primarily incises in screes, limestones and dolomites (Table 2) corresponding to 46% and 48% of the surface catchment respectively. The upper portion of the torrent acts as a by-pass zone, with exposed bedrock and minimal sediment cover (Fig. 2A). Downstream, the Dente torrent merges with other torrents in the Vievola catchment, feeding the Vievola alluvial fan, which was re-activated during Storm Alex (Kerverdo et al., 2025; ONF-RTM, ONF-DRN, INRAE-ETNA, 2023).

The Consciente torrent lies adjacent to the Vievola catchment, just

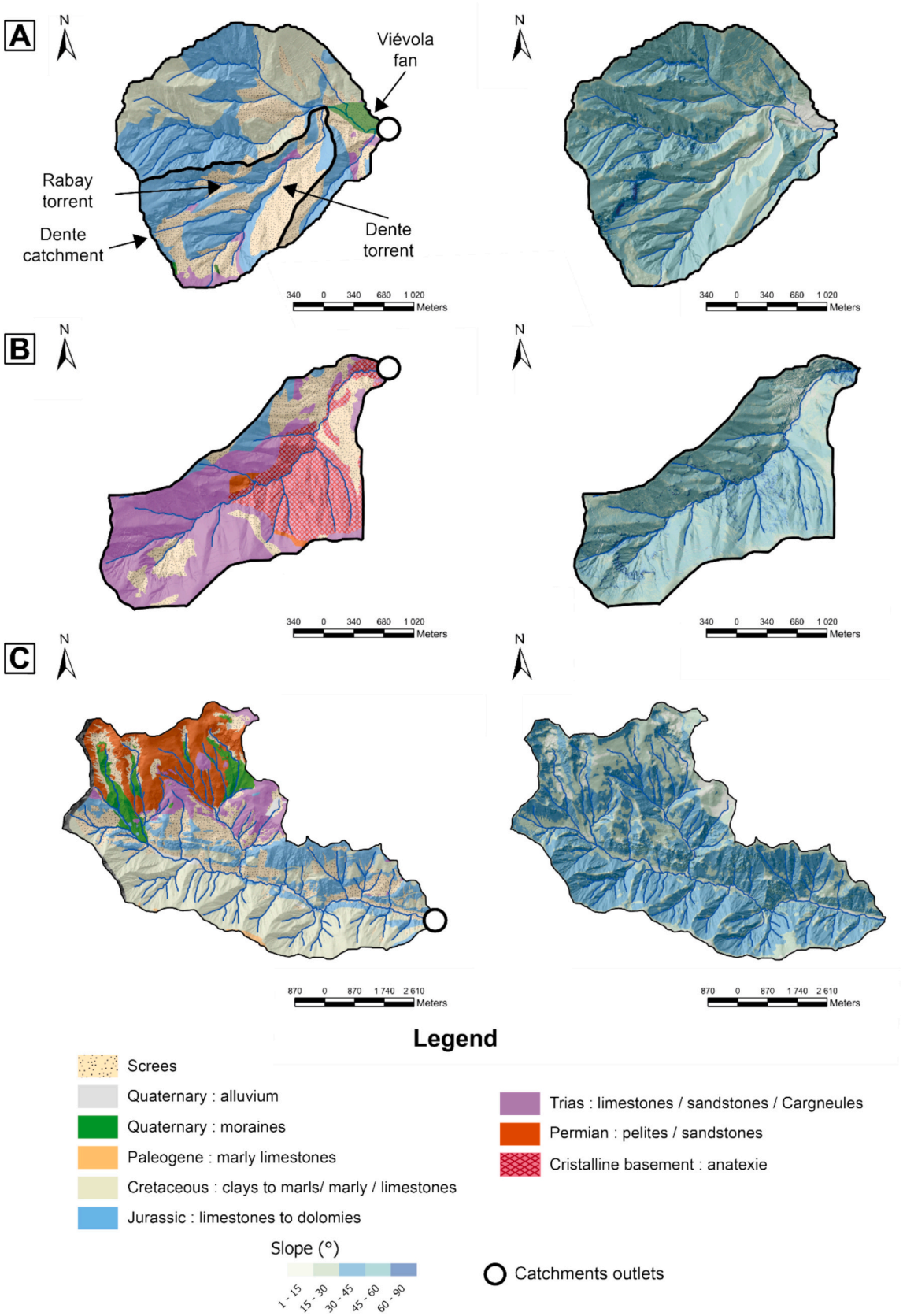

Fig. 2. From A) to C): Vievola, Consciente and Cairos catchments. Left panels correspond to simplified geological maps derived from BRGM 1:50,000. The right panels show slope maps classified into five classes based on slope angle (in degrees): 1–15°, 15–30°, 30–45°, 45–60°, and > 60°. Catchment outlets are indicated by white circles.

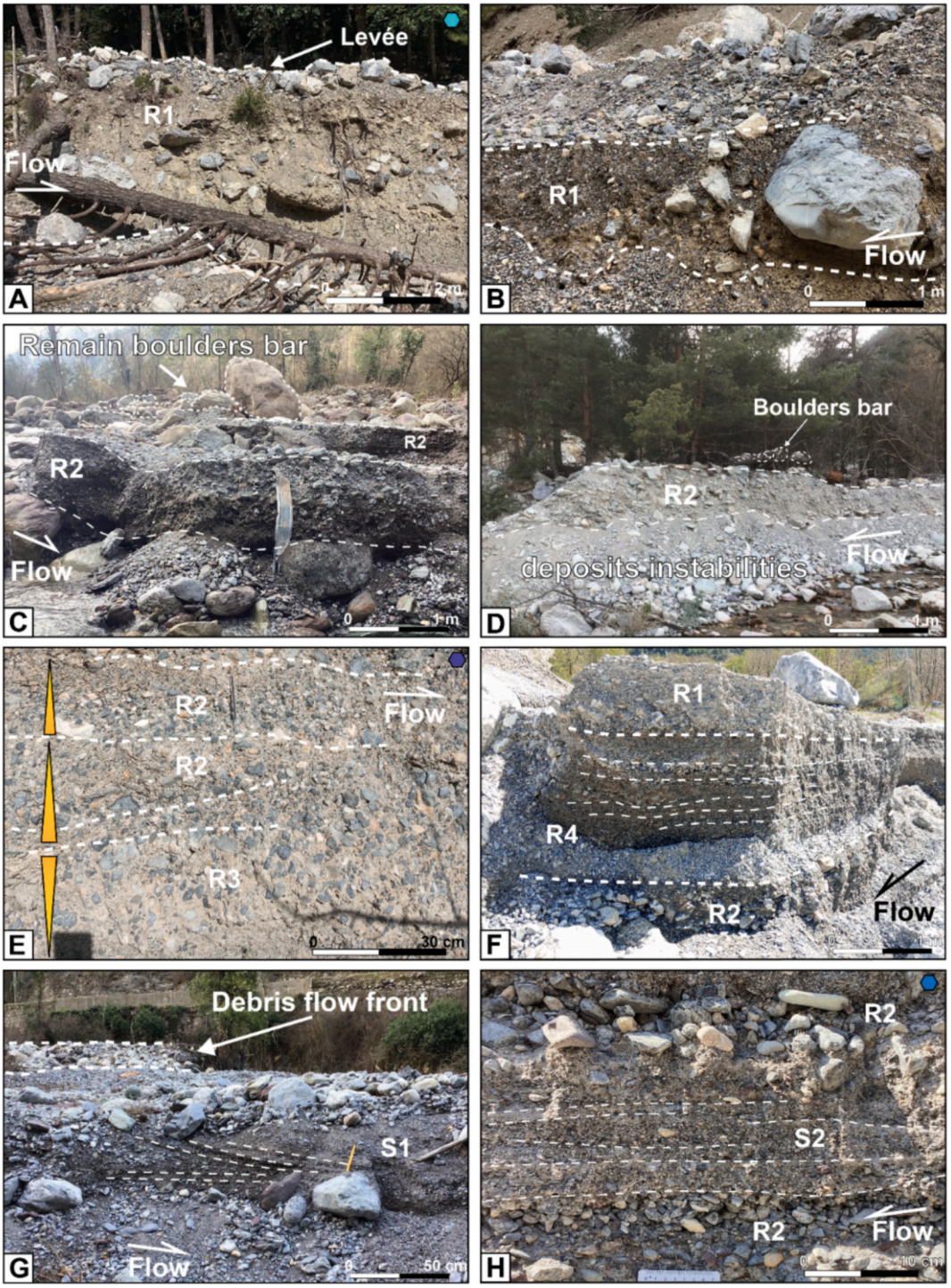

Fig. 3. Photographs of deposits identified at various locations in the Roya Valley following Storm Alex. (A), (B) Debris-flow deposits (lithofacies R1) in the Dente torrent. (C—D) formed by tractive-currents deposits, characterised by boulder bars (lithofacies R2). (E) Lower part of the section showing inverse grading, overlain by normal grading (R3 then R2). (F) Association of lithofacies R2, R4, and R1 on the Vievola alluvial fan. (G) Trough cross-stratification (S1). (H) S2 deposits with planar laminations and sand lenses. Blue dots in the upper right corners of panels A, E and H indicate the locations of the sedimentary logs shown in Figs. 4 and 8.

Table 1
Main characteristics of the three studied catchments. Their locations (see Fig. 1), morphometric parameters, and the average 24-h rainfall recorded on 2 October 2020.

Catchments	Area (km^2)	Perimeter (km)	Length (km)	Max. relief (m asl)	Min. relief (m asl)	Denivelation (m)	Mean slope (%)	Rainfall Alex Storm (mm/24 h)
Dente	2.4	7.01	3	2281	1013	1268	73	547
Consciente	4.2	9.8	3.8	2199	903	1296	70	588
Cairos	42.1	34.4	10.6	2681	386	2295	70	323

Table 2
Lithologies cover on the surface catchment expressed in %.

Catchments	Lithological composition of the studied catchments (%)							
	Screes	Moraines	Limestones and dolomites	Marls, marly-limestones	Clay / Cargneules	Sandstones	Migmatites	Others
Dente	46.4	0.2	48.1	0.4	4.7	–	–	0.2
Consciente	19.6	–	42.8		3.6	5.8	28.2	–
Cairos	19.3	5.5	20.6	31.2	1.1	19.3	–	3

south of the Dente torrent (Figs. 1 and 2B). It received the highest cumulative rainfall during the event, totaling 588 mm in 24h (Table 1). Covering 4.2 km^2, the Consciente torrent extends 3.8 km in length. Elevation ranges from 2199 m a.s.l. to 903 m a.s.l (Fig. 2B, Table 1) and is characterised by steep gullies, with a mean hillslope gradient of 70% (Fig. 2B, Table 1). Lithologically, the Consciente catchment differs from its neighboring Dente catchment (Fig. 2B). It can be divided into two main parts: (1) the upper section is composed of limestones, sandstones and migmatites from the Argentera-Mercantour, (2) the lower section consists of screes and Triassic cargneules (Fig. 2B). In surface comparison, limestones and dolomites represent 48% of the surface, migmatites 29%, screes 20% and the remaining 3% comprises various other lithologies (Table 2).

The Cairos River (Fig. 2C) is located on the right bank of the Roya River (Fig. 1). It received less rainfall during the event, with an estimated 323 mm in 24h (Table 1). Spanning 42.1 km^2, the Cairos is one of the largest catchments in the Roya Valley, with a channel length of 10.6 km (Table 1). Its upper reaches rise to 2681 m a.s.l. (Fig. 2C, Table 1). The valley floor is relatively flat and the Cairos has incised terraces dated from the Wurm period (Gèze and Nesteroff, 1996; Julian, 1977). The mean hillslope gradient is 70% (Table 1). Jurassic limestones form cliffs that delimitate the valley floor (Fig. 2C). Lithologically, the Cairos catchment can be divided into two sections, separated by the main river channel (Fig. 2C). The northern section consists of Permian sandstones (19% of the surface, Table 2) and Jurassic limestones (~21% of the surface, Table 2,Fig. 2C), along with moraines and screes from the last glacial period (~24% of the surface), producing steeper slopes than those in the south (Fig. 2C, Table 2). In contrast, the southern section is largely composed of Cretaceous marly-limestones dissected by numerous torrents (Fig. 2C) accounting for 31% of the surface (Table 2).

3. Data and methods

3.1. Morphometric characteristics of rivers and torrents

Cartography of the active channels before and after Storm Alex was carried out in ArcGIS Pro, based on aerial imagery and LiDAR data from post-event surveys conducted by the French National Institute of Geographic and Forest Information (IGN, Table 3). Mapping of the modern valley floor (or valley width in steep torrents) follows the methodology used in recent post-flood analyses (Liébault et al., 2024; ONF-RTM, ONF-DRN, INRAE-ETNA, 2023).

In the Roya Valley, the absence of pre-flood LiDAR data (Table 3) limited the mapping to post-event datasets. For the Cairos River, only the post-flood valley floor was digitized. A 10 m threshold from the current channel margins was used to distinguish relict terraces from modern fluvial deposits, an approach commonly applied to valley floors mapping in the Rhone basin and Mediterranean margins (Alber and Piégay, 2011), and validated by Liébault et al. (2024).

For narrow torrents such as Dente and Consciente, the entire valley width was digitized. Polygons representing the valley floor and active-channel zone were segmented into 200 m-long reaches. The modern valley-floor polygon was used as a reference to delineate the active channel, and a centerline was generated for each segment in ArcGIS Desktop using the Fluvial Corridor plugin (Roux et al., 2015).

From the IGN LiDAR HD dataset (IGN, 2023a), we extracted the mean valley width, channel width, and slope for each 200 m reach. A $Width_{after}$ / $Width_{before}$ ratio (Krapesch et al., 2011) was calculated to quantify the extend of channel widening after the flood. The Confinement index (Comiti et al., 2016b), defined as the ratio between the modern valley-floor width and the pre-flood active-channel width, was also computed for each reach. Following the classification of Ruiz-Villanueva et al. (2023), three confinement categories were applied: 0–2 = confined; 2–4 = partially confined; >4 unconfined.

The absence of a high-resolution pre-event DTM prevented the rapid generation of a Difference of DEMs (DoD). Only a Digital Surface Model (DSM) derived from the photogrammetric processing of IGN aerial imagery acquired in July 2020 was available (Table 3), providing a surface model of sufficient resolution (IGN, 2023b). As a result, comparisons could only be made in areas with sparse or no vegetation (Kerverdo et al., 2025).

Bed-level changes were manually estimated in ArcGIS Pro by selecting points located within unvegetated areas of the inner channel. Elevation values were extracted from the DSM_{2020} and DTM_{2020}, and the differences between them were calculated. The resulting values of bed-level change were then projected onto the post-flood active-channel centreline using the *Locate Features Along Routes* tool in ArcGIS Pro.

3.2. Fieldwork

3.2.1. Outcrop analysis

Three field campaigns (March, June, and October 2023) were carried out to characterise deposits exposed in intact outcrops along the Roya hydrological network most affected by the storm. This included photographic documentation of six outcrops and the construction of sedimentary logs. Twenty-three representative horizons were sampled to analyse the grain-size distribution of the finer fraction of the matrix. Sample masses ranged from ~350 g to 1 kg. In the case of very thin

Table 3
Data used to determine morphometric parameters of the rivers and torrents. Most datasets were acquired by IGN (IGN, 2020; IGN, 2023a; IGN, 2023b). The DSM_{2020} from MNS Correl has an vertical accuracy precision of ~0.2 m and a resolution of 0.5 m/pixel. The DTM_{2020}, covering the main valleys, offers an vertical accuracy of ~0.1 m, a planimetric precision of 0.5 m, and 1 m resolution. Its coverage is limited to the main course of the Roya and the lower reaches of the Cairos, Dente, and Consciente torrents. The DTM_{2021} has an altimetric precision of 0.1 m and a planimetric precision of 0.5 m.

Type	Name	Source	Acquisition Method	Date	Resolution
Ortho-images	BD Ortho®	IGN	Aerial image	July 2020	20 cm/pixel
Ortho-images	BD Ortho Express®	IGN	Aerial image	October 2020	20 cm/pixel
Ortho-images	Study data	Study acquisition	UAV Coverage	2023	1 cm/pixel
DSM_{2020}	MNS Correl®	IGN	Correlation by ortho-images	2020	50 cm/pixel
DTM_{2020}	NUADLID®	IGN	LiDAR (post-event survey)	October 2020	1 m/pixel
DTM_{2021}	LiDAR HD®	IGN	LiDAR	2021	1 m/pixel

horizons, only the central portion was collected, to avoid potential contamination from adjacent layers. The maximum particle size (a-axis) was measured in situ.

For each 200-m river segment, wherever possible (considering accessibility, water level, etc.), the maximum size of boulders mobilised by the storm was also measured. If direct measurements were not feasible (e.g. unsafe to access), boulder dimensions were estimated using very high-resolution drone imagery.

Any notable sedimentary structure (e.g. boulder bars, debris flow fronts), as well as measurement points, were geolocated via GPS with the Clinomove app. All data were stored in KMZ format for use in Google Earth or within GIS software.

3.2.2. UAV surveys

To obtain orthophotographs for areas not covered by IGN aerial surveys after Storm Alex (Table 2), several UAV (Unmanned Aerial Vehicle) flights were conducted using a Matrice 3E Enterprise drone equipped with RTK (Real-Time Kinematic). The RTK module ensured centimetre-scale positional accuracy. Imagery was processed with Agisoft Metashape 1.8.3, resulting in orthomosaics with a mean resolution of approximately ~1.5 cm/pixel (Table 2).

3.3. Sedimentological analysis

Grain-size analyses combine sieving for particles >80 μm and laser diffraction for finer fractions. Samples are oven-dried at 60 °C for 24 h, then sieving at mesh sizes of 0.08, 0.25, 0.5, 1, 2, 5, and 10 mm for 15 min at a frequency of 0.8. Each fraction is weighed separately. Material <80 μm is analysed with a Beckman Coulter LS 13320 XR laser diffractometer (0.04–2000 μm range). We derived percentages of sand (>63 μm), silt (4–63 μm), clay (<4 μm), as well as the median grain size (D_{50}) and mode, using the GRADISTAT software (Blott and Pye, 2001). All data are compiled in Excel spreadsheets and then imported into GRADISTAT for statistical analyses.

3.4. End-member flow maps

Flow maps are produced to illustrate the dominant flow conditions during Storm Alex based on the end-member deposits observed in the field. These maps show the spatial variability of flow types at 200 m intervals, where feasible (section 3.1).

They are primarily based on the interpretation of field observations such as: debris flow fronts, levees, boulder bars and on occasional subsurface analyses including stratigraphic logs and grain-size distributions. The maps distinguish several key flow regimes: bedload-dominated deposition zones, debris flow deposits, sheet-floods or massive lateral inputs, reaches with intense channel widening, bypass zones. Intense widening is identified using a width ratio threshold of 2.5, as proposed by Ruiz-Villanueva et al. (2023), which corresponds to the most significant widening observed in Mediterranean catchments affected by large and extreme floods. By synthesising these various field data, the flow maps provide an integrated and spatially explicit overview of the flow heterogeneity and sediment transport dynamics during the Storm Alex.

4. Results

4.1. Lithofacies associations

From the studied outcrops across the different valleys, we identified six distinct lithofacies (R1 to R4 and S1 to S2) within the deposits of the Alex flood (Fig. 3). The principal sedimentary structures such as sorting, grading, clast imbrication, bedding and the geometry of observed intervals are summarised in Table 3 and illustrated in Figs. 4–8. The transitions between debris flows (R1), bedload-dominated deposits (R2), and more dilute hyperconcentrated or sheet-flood conditions (R3, R4) are analysed by examining each torrent (Table 4). These transitions reflect shifts in flow energy, sediment concentration, and local topographic confinement, with processes ranging from bedload-dominated transport (R2) to sheet-flood (R4), and ultimately debris flows (R1) depending on sediment supply and flow rheology.

4.1.1. Dente torrent and Vievola fan

The torrent was studied from upstream to downstream along its full course (Fig. 4, logs D5K to D2K), as well as on the alluvial fan (log D1K). The main field observations are summarised below.

The upstream deposits particularly in logs D5K and D3K (Fig. 3A and B), are dominated by lithofacies R1. Log D4K displays vertical variability, with the emergence of lithofacies R2, characterised by an openwork texture, clast imbrication, and clasts aligned parallel to the flow direction. The maximum particle size (MPS) reaches up to 1 m in logs D5K to D3K (Fig. 4C-F).

Further downstream, at the Dente torrent (log D2K, Fig. 4F), the base of the deposits consists of lithofacies R3, overlain by R2 units (Fig. 3E). These facies associations are observed near the channel margins. Facies R3 exhibits inverse grading about 20 cm thick, overlain by three normally graded layers, each 15–20 cm thick.

On the Vievola fan, log D1K (Fig. 5) shows a basal R3 unit overlain by a lower interval dominated by a coarsening-upward R4 unit, capped by thin (15 cm) R2 deposits (Fig. 5D and E). Clasts range from rounded to angular, with MPS values increasing from ~10 cm in the upper fan to 40–50 cm downstream (Fig. 8E). The upper half of log D1K displays three R2 horizons, each forming a wedge-shaped body that widens downslope (Fig. 5D). This geometry suggests a transition from bedload to more cohesive flow deposits.

The flow appears to have been constrained by the presence of a railway bridge approximately 11 m wide and 10–12 m high (Fig. 5A-C). The accumulation of massive deposits and progressive infilling beneath the bridge likely influenced flow dynamics and controlled the geometry of deposits within the main channel, potentially explaining the observed lithofacies variability.

Laterally to log D1K, within the main channel feeding the fan, a single lithofacies is observed: R4 (Fig. 6). It consists of a succession of rhythmic couplets displaying normal grading from pebbles to coarse sand (Fig. 3F), with locally developed scour-and-fill structures (Fig. 6A). Clasts are angular and show moderate to well-developed imbrication.

Most of the R4 lithofacies appear to blanket the entire fan surface (Fig. 6B), while the active channel is represented by log D1K (Fig. 5).

Grain-size analysis reveals a higher fines content in R1 compared to R2, R3, and R4 (Table 3). Comparison of two bulk lithofacies R1 samples with R2 – R4 layers from the three catchments indicates an average increase of approximately 5 wt% in fines for R1, consisting +1.3–5.7 wt % silt and + 0.3–0.7 wt% clay (Table 3).

4.1.2. Consciente torrent

In the Consciente valley, the impact of Storm Alex was investigated at the outcrop shown in Fig. 7, where extensive bank erosion resulted in the formation of multiple small terraces (Fig. 7B and C). Observations from each terrace (Fig. 7C and F) indicate that the deposits either lack clear grading or display normal grading. From base to top, the succession comprises lithofacies R2 and R3 (Fig. 7D and F).

The lower terrace (T5) consists of large clasts with strong imbrication (dip ~60°) and a thickness of ~1 m (Fig. 7F). Terraces T4, T3 and T2 (highlighted in yellow in Fig. 7F) are interpreted as R3 lithofacies, with poorly sorted, grain-supported gravels and limited imbrication (Fig. 7F). Terrace T1 exhibits normal grading, with an upward transition from R2 to R3 (Fig. 7F).

The uppermost terrace (Tf) is composed solely of blocks measuring several tens of centimetres across, with a poorly preserved or entirely absent matrix (Fig. 7F).

Grain-size analyses of the interclast matrix (Table 3) reveal a composition dominated by pebbles (47.7–91 wt%) and coarse sand

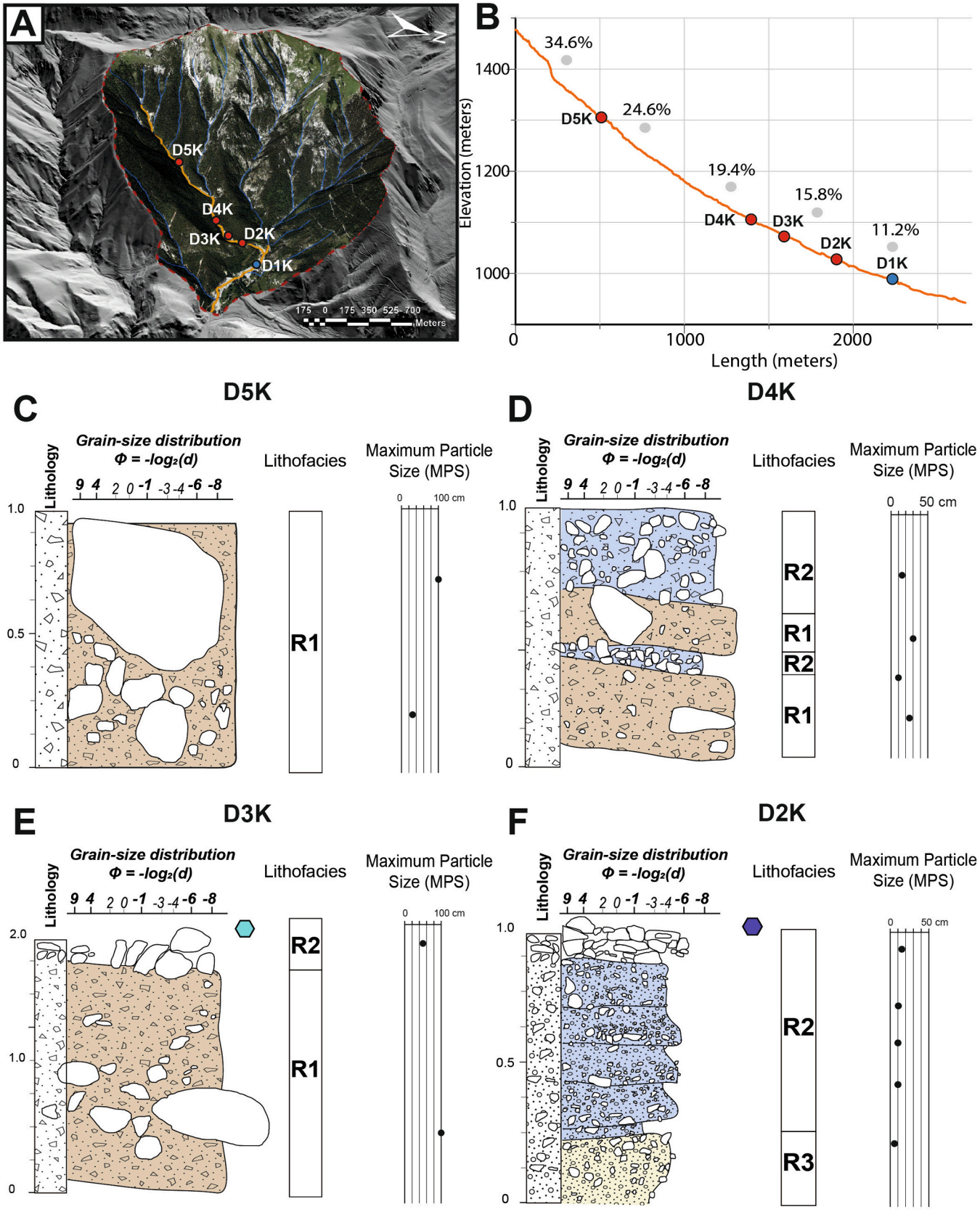

Fig. 4. Stratigraphic survey of the Dente torrent. A) LiDAR hillshade and orthoimages of the study area from (IGN, 2023a), the orange line marks the torrent course. B) Red dots indicate the locations of the stratigraphic log (C, D, E, F). The blue dot corresponds to the Vievola fan log (described in the next figure). Light blue and dark purple hexagons mark in the upper right corners of panels D and F refer to the photo locations shown in Fig. 3A and E. Gray dots indicate the mean slope calculated every 500 m.

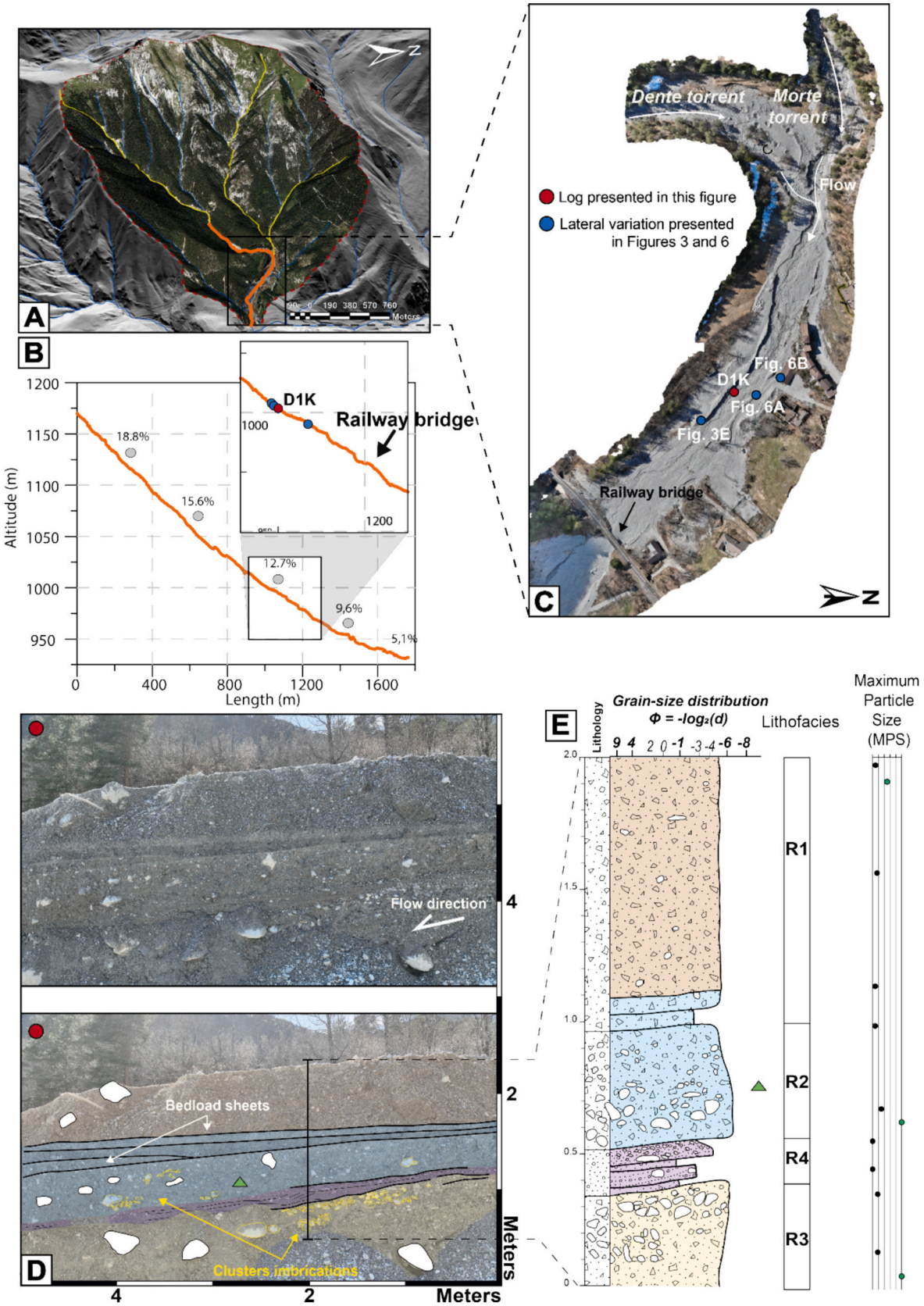

Fig. 5. Stratigraphic observations in the Vievola alluvial fan. A) LiDAR hillshade and orthoimage of the study area from (IGN, 2023a). B) Longitudinal profile of the Dente torrent, extending downstream to its confluence with the Roya River. C) UAV image acquired in April 2023 showing the investigated sites on the Vievola fan. D) Photographs illustrating the channel margin of the fan. E) Stratigraphic log corresponding to the outcrop shown in panel D. Blue dots on the MPS scale indicate clasts measured along the longitudinal profile, whereas black dots correspond to clasts visible in panel D. The green triangle marks the location of a grain-size sample.

Fig. 6. Sheet-flood deposits on the left bank of the Vievola channel (Fig. 5C). A) Sheet-flood deposit reaching up to ~ 2 m in thickness. Downstream, a 1 m-wide channel filled with gravel crosses the deposit perpendicularly. B) Sheet-flood deposit behind a building, showing normal grading and increasingly rhythmic couplets upward. The coarser layers exhibit openwork textures and strong imbrication.

(8.6–48 wt%), with a minor fine fraction (coarse silt = 0.5–4.3 wt%, clay = 0.06–0.37 wt%). These results, combined with stratigraphic observations, indicate the presence of multiple boulder bars, 1–3 m wide and 1–2 m high, extending from metric to decametric scales. The largest clasts reach 2–5 m in length. These boulder bars are aligned parallel or oblique to the flood flow within the inner channel (white arrow in Fig. 7C).

4.1.3. Cairos River

Stratigraphic observations along the Cairos River are limited (Fig. 8), focusing primarily on the uppermost part of the Alex-related deposits, based on three logs C1K to C3K.

Log C1K (Fig. 8C) located within a short gorge section, represents overbank deposits. It consists of three normally graded layers with a total thickness of 2 m. The basal layer is composed of cobbles and pebbles exhibiting upward fining and corresponds to lithofacies S2. The second layer has a planar and sharp base, with a matrix dominated by coarse pebbles and displaying upward fining and planar stratification. The third layer is bounded by an erosional surface and lacks visible grading. All clasts are imbricated, and the bedding is horizontal.

Log C2K (Figs. 3H and 8D) corresponds to the uppermost part of the channel-fill deposits. This outcrop was shaped during the recession phase and shows slight incision into the main channel deposits. It comprises four layers: three belonging to lithofacies R2 and one to lithofacies S2, the latter characterised by trough cross-stratification (Fig. 3G). The total thickness is around 1 m, with individual layers ranging from 20 to 30 cm. Strong clast imbrications are present, with dip angles around 30–35°. All layers, except the sandy one, exhibit normal grading.

Log C3K (Fig. 8E), located on an alluvial fan at the Cairos–Roya confluence, differs from the Vievola fan deposits (Fig. 5). It comprises three normally graded layers with a coarse, pebble-rich matrix. The maximum particle size (MPS) within the matrix reaches up to 15 cm. Stratified horizons dip at angles between 20° and 35°.

The matrix across all Cairos logs is generally dominated by coarse sand and pebbles, with pebble content ranging from 47 to 81 wt%, sand from 8 to 43 wt%, and fines (silt + clay) between 0.5 and 5 wt%. Clay content ranges from 0.05 to 0.2 wt% (Table 3).

4.2. Morphometric changes

Sedimentological observations were complemented by morphometric analyses conducted at several locations along the rivers. Reach-scale metrics such as slope, bed-level variations, and channel width were used to further constrain the geometry and sediment dynamics of the deposits described in the previous section (Fig. 9).

4.2.1. Dente torrent

The Dente torrent was divided into 15 Sections, each 200-m in length (Fig. 9A). Section 1 is located at the highest elevation, while section 15 corresponds to the lowest point. The torrent displays a steep longitudinal profile, with an average slope of ~21%. The mean Confinement index (Ci) is 4.6 for Sections 1 to 11 (Sections 12 to 15 were excluded due to the unconfined environment of the Vievola fan).

In Sections 1 to 5, the channel is confined (Ci = 2.4) within Jurassic limestones, with an average slope of 33%. Before the event, the channel width varied between 4 and 5 m. In Sections 6 to 11, the channel borders lithologies composed mainly of scree and fluvio-glacial outwash deposits, with an average slope of 19% and a higher confinement index (Ci = 6.4). Compared to upstream, the channel widens slightly, ranging from 5 to 8 m. Section 7 is an exception, corresponding to a 200 m-long gorge incised into Triassic limestones.

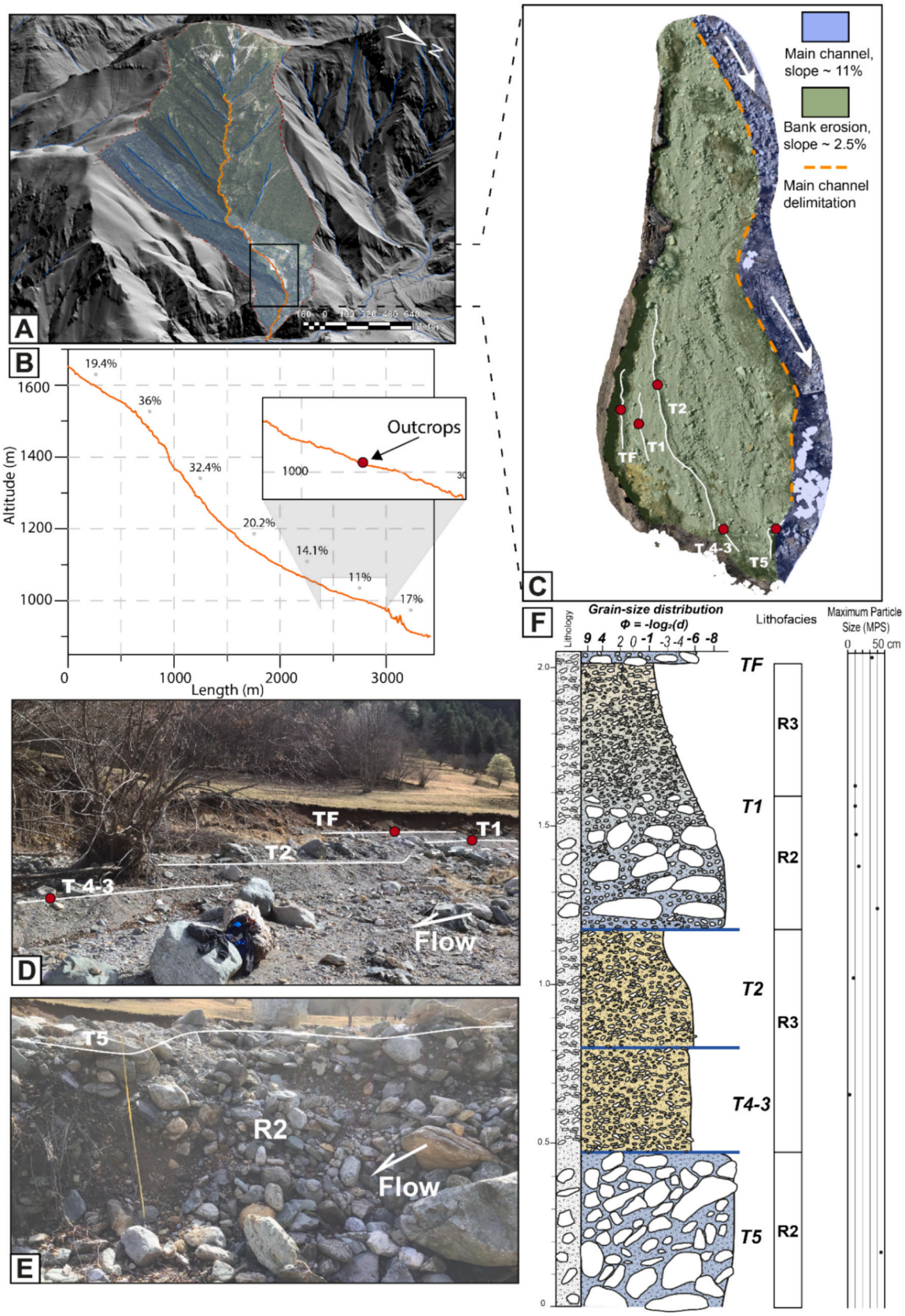

Fig. 7. Stratigraphic observations from the Consciente torrent. A) LiDAR hillshade and orthoimage from the area from (IGN, 2023a). B) Longitudinal profile of the Consciente torrent, highlighting outcrops D, E and F. C) UAV image acquired (March 2023) showing the area and the location of remnants terraces. D) Photographs of terraces taken after the flood. E) Base of the section shown in panel F, featuring cobble- to boulder-sized deposits with openwork textures and clear imbrications. F) Composite stratigraphic log of the terrace sequence with unit boundaries marked by blue lines.

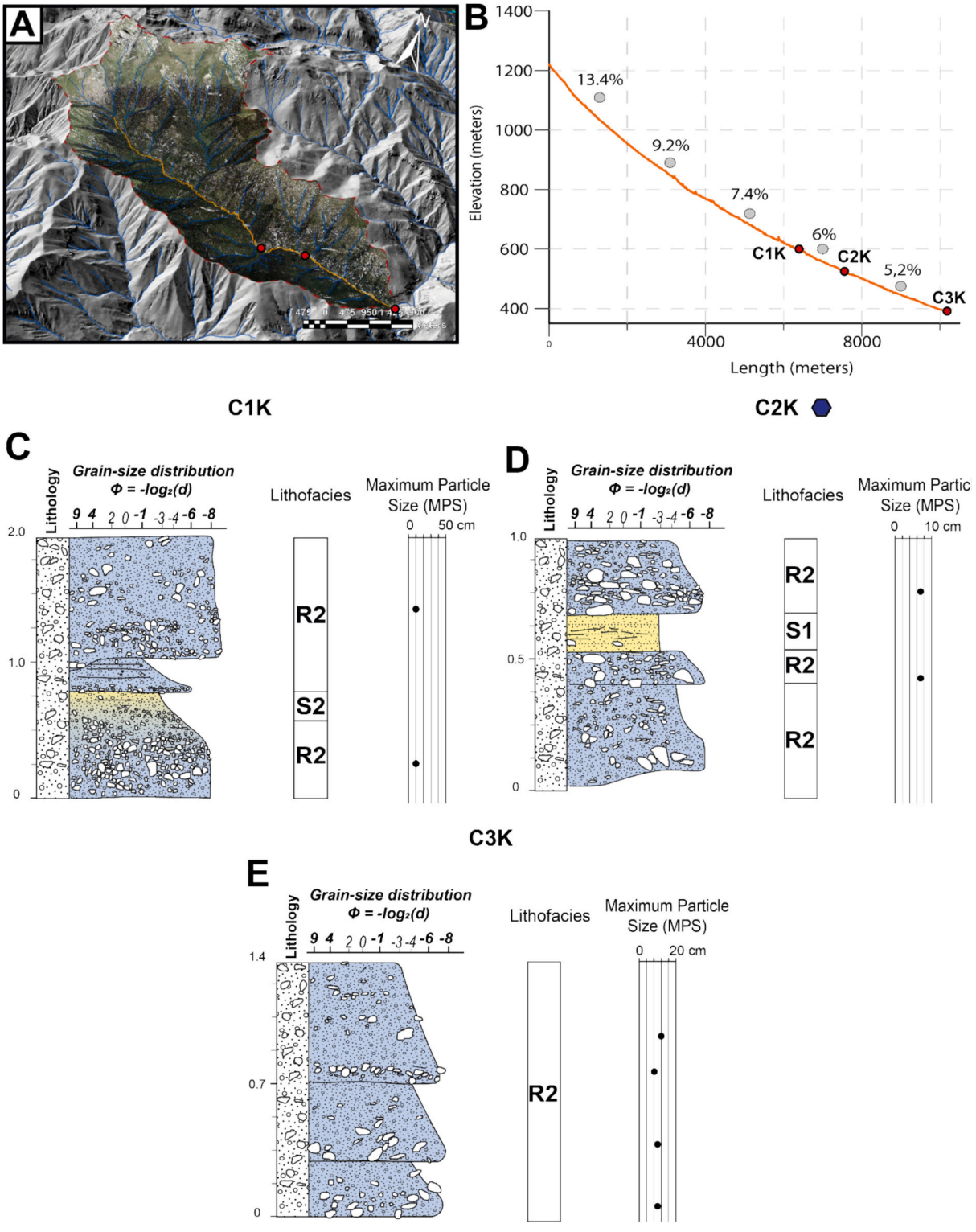

Fig. 8. Stratigraphic logs from the Cairos River. A) LiDAR hillshade and orthoimage of the studied area from (IGN, 2023a). B) Longitudinal profile of the Cairos River showing the location of the outcrops C, D and E. (C, D, E) stratigraphic logs described along the river, as indicated on the longitudinal profile in panel B. Dark blue hexagons mark in the upper right corners of panel D refer to the Fig. 3H.

Sections 12 to 15, cross the Vievola alluvial fan, where the channel width ranges from 5 to 7 m, and slope decreases to ~10% (Fig. 9A). This downstream reach is anthropised and artificially channelised.

Following the flood, the average width ratio is 6.2, indicating mean widening from 6 m to 36 m (see supplementary material 2). Widening becomes particularly marked from section 8 onwards, reaching ~59 m near sections 9 to 15 (Fig. 10). The widest zone corresponds to the fan apex and the Roya confluence (Fig. 3A).

The upper reach of the Dente torrent exhibits net incision, with depths ranging from ~ − 4 m to ~ − 1 m (Fig. 9A). The most significant incision is recorded in Sections 1–2 (Ci = 1.2) and 7–8 (Ci = 3.7). In contrast, Sections 3 and 8 show minimal elevation change, suggesting

Table 4
Table of the six lithofacies described after Storm Alex in the Roya Valley. Lithology, sedimentary structures, dimensions, grain-size distribution and interpretation are given. Each lithofacies are interpreted on the base on the literature.

Code	Lithology	Sedimentary structrures	Dimensions	Grain-size distribution	Interpretation
R1	Massive, structureless conglomerates of cobbles to boulders in a sandy-gravelly matrix	Ungraded to normally graded layers; clast-supported or matrix-supported; disorganized clast orientation, boulders front, levees	Thickness: 20–50 cm to ~1 m; isolated boulders 80 cm–2 m; extent: several decametres downstream	65–78 wt% pebbles 12–20 wt% sand 3.6–8.6 wt% silts 0.4–1.3 wt% clay Unimodal distribution centered on medium pebbles (D_{50} ≈ 9 mm)	Characteristic of debris flows (Costa, 1984; Iverson, 1997; Lowe, 1982). Low clay content (~1 wt%) suggests granular debris flows, indicating limited cohesion but high interstitial pressure and buoyancy (Hampton, 1979; Iverson, 1997; Middleton and Hampton, 1973)
R2	Massive, clast-supported openwork conglomerates with coarse sand to pebble matrix	Sub-horizontal; faintly stratified beds; normal grading; strong imbrication (dip angles 40–60°); boulder bars; overbank deposits	Thickness: 1–2 m; Lateral extent: several hundred metres	47–81 wt% medium to coarse pebbles 8–43 wt% and 0.5–5 wt% silts; 0.05–0.2 wt% clay; Median grain size (D_{50}): Cairos ≈6.5 mm, (D_{50}) Consciente ≈7.0 mm, (D_{50})Vievola ≈7.6 mm.	Strong clast imbrication, openwork textures, and normal grading suggest bedload transport in high-energy, Newtonian flows or debris-floods (Brenna et al., 2024; Brenna et al., 2020; Church and Jakob, 2020; Frey and Church, 2011; Hungr et al., 2014; Hungr et al., 2001). Variations orientation and dip angles reflect changes in shear stress and sediment supply.
R3	Matrix- to clast-supported deposits	Ungraded or inversely graded; moderate stratification; sandy base overlain by pebble-rich tops	Thickness: 15–40 cm; Lateral extent: few metres to several decametres	~77 wt% pebbles ~20 wt% sand 0.5–5 wt% silts; 0.05–0.2 wt% clay Unimodal distribution centered on medium pebble D_{50} ≈ 11.9 mm	Inverse to normal grading and moderate stratification suggest hyperconcentrated flows (Pierson; 2005a). These flows have high sediment concentrations but lack the full cohesion of debris flows. The inverse grading arises from traction carpets and intense shear near the bed (Sohn, 1997)
R4	Clast-supported gravels (granules to pebbles) and coarse sand layers	Rhythmic alternation of coarse gravels and sand layers; weak imbrication; partially openwork textures; near horizontal bedding with 1°–3° dips; occasional cross-bedding.	Coarse units: 20–50 cm; Sandy layers: 10–30 cm; Couplets: 30–80 cm; Lateral extent: tens to hundreds of metres downstream	58–93 wt% pebbles 4–41 wt% sand 0.5–1.3 wt% silts; 0.04–0.2 wt% clay Unimodal distribution centred on medium pebble (D_{50}): ≈7.6 mm;	Rhythmic alternation, planar bedding, and partial to fully openwork textures (in some cases with cross-beds) are typical of sheet-flood processes (Blair, 1987, 2000; Blair and McPherson, 1994). These often develop in less confined, possibly fan-like zones under supercritical-flow conditions. The alternation between coarse and fine-grained layers likely reflects fluctuating discharge and sediment availability
S1	Sandy to gravelly, matrix-supported layers; sub-angular clasts oriented parallel to flow	Faint (quasi-trough) cross-stratification; partially openwork textures; erosional base with imbricated pebbles	Thickness: 20–40 cm; Lateral extent: several hundred metres		Exhibits faint cross-stratification and coarse sands-granules interbeds, consistent with subcritical flow under relatively high sedimentation rates. Trough cross-stratification (Ashley; 1990) suggests turbulent; non-cohesive conditions that allow ripples migration and rapid deposition (Venditti et al.; 2005)
S2	Medium sand to medium pebbles, poorly to moderately sorted		Thickness: 15–20 cm; Lateral extent: not specified		Lens-shaped strata with normally graded sand-to-pebble beds, reflecting small-scale bar migration under high-energy conditions (Allen, 1982; Ashley, 1990; Miall, 1996). Coarser material is deposited during peak flows, followed by fining-up as flow energy wanes

alternating erosion and local infill. From Sections 9 to 13, corresponding to the Vievola fan, net aggradation is observed, averaging between +2 m and + 4 m.

Section 5 (Ci = 2.9) corresponds to the confluence with the Rabay torrent. Approximately 46,000 m^3 was delivered at this position due to landslides and the flushing of gullies in the headwaters of the sub-catchment (Kerverdo et al., 2025). Bank erosion between Section 6 and 12 produced ~57,000 m^3 of sediment, with an additional ~36,900 m^3 contributed from the headwaters of the Dente torrent (Kerverdo et al., 2025).

Two dominant lithofacies are observed in the Dente torrent: R1 and R2 (Fig. 9A). R1 end-member deposits are located in areas of slope reduction and pronounced channel widening (mean Ci where R1 is observed = 4.9). For instance, in Section 3, the slope decreases from 49% to 29%, where log D5K is situated. Surface R1 features include levees and massive, ungraded boulder lobes (Fig. 10A), notably in Section 6, where significant widening occurs (width ratio × 6), and immediately upstream of constricted segments such as Section 7 (the gorge segment). Sections 8–9 also show substantial widening (width ratio ~ 4, Ci = 5.3) and a decrease in slope.

Lithofacies R2 is represented by boulder bars and imbricated clast structures, mainly observed in Sections 1–2, 4, and 6 (Fig. 10A). From Sections 9 to 15, surface and stratigraphic observations reveal a combination of R2–R4 deposits, with localised occurrences of R3 and R1 end-member facies (Fig. 10A). These deposits are found across both steep and gentle slope domains and are frequently interbedded (Fig. 4).

4.2.2. *Consciente torrent*

The Consciente torrent was divided into 19 Sections (Figure 9B), with Section 1 located upstream and Section 18 downstream at the confluence with the Roya River (Fig. 10B). For Fig. 9, Section 19 is not considered because it is shorter than the other sections. The average longitudinal slope is ~30% and the mean confinement index is 3.

The slope increases from ~22% in Sections 1–4 (pre-flood channel width ~ 6 m, Ci = 2.7) to ~43% in Sections 5–11 (Ci = 1.6), coinciding with a lithological transition from Jurassic limestones and sandstones to a gorge incised into the migmatites of the Argentera–Mercantour basement.

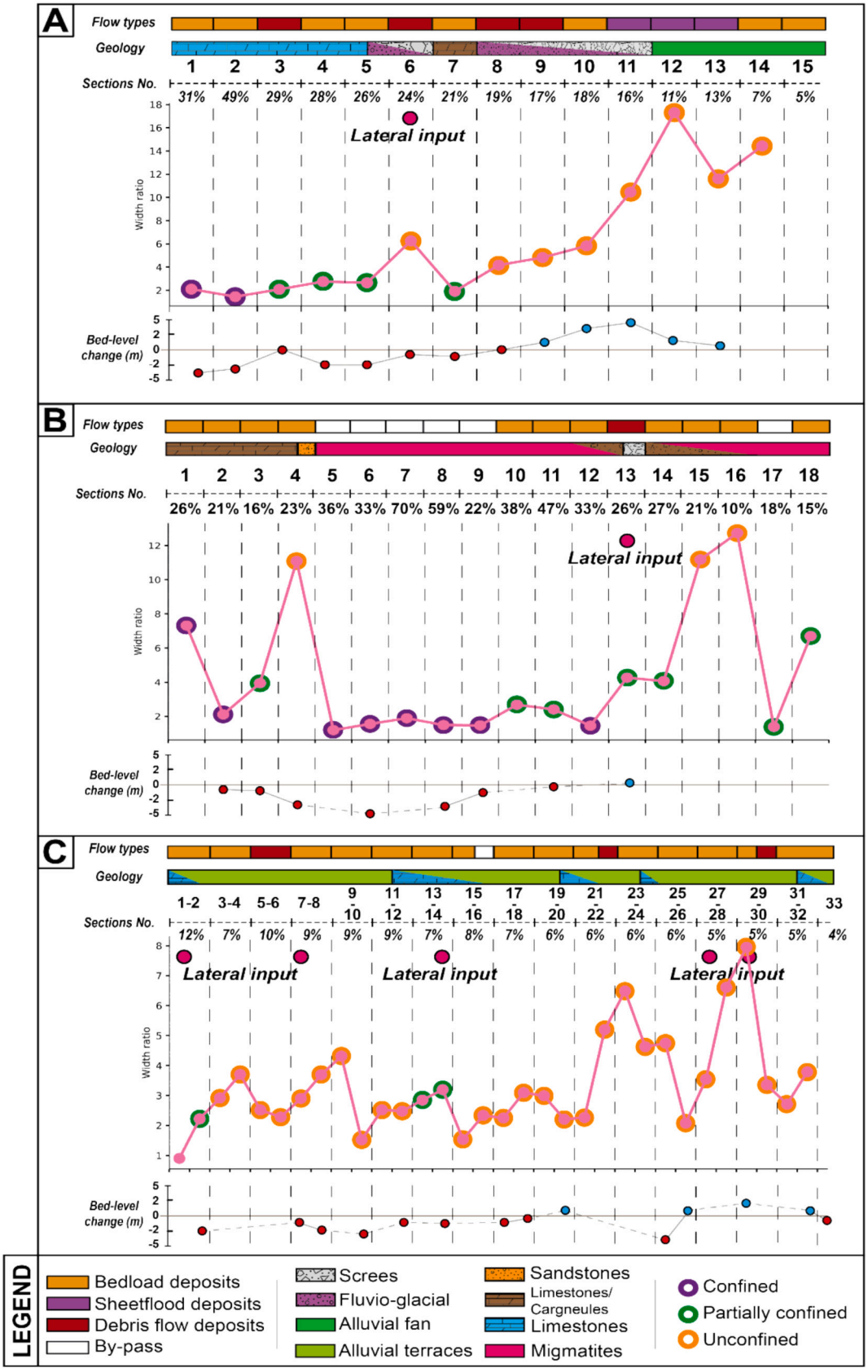

Fig. 9. Longitudinal sections of the studied torrents (200 m segment length). The flow-type panel illustrates the dominant depositional processes identified in the field, whereas the geology panel indicates the lithologies encountered along each torrent. The mean slope for each section is expressed in percent. The pink curve shows the variation of the width ratio, with the surrounding colour shading indicating whether each reach is confined, partially confined, or unconfined. The lower panel displays bed-level changes where data are available. Labels (A), (B) and (C) correspond to the Dente, Consciente and Cairos catchments, respectively.

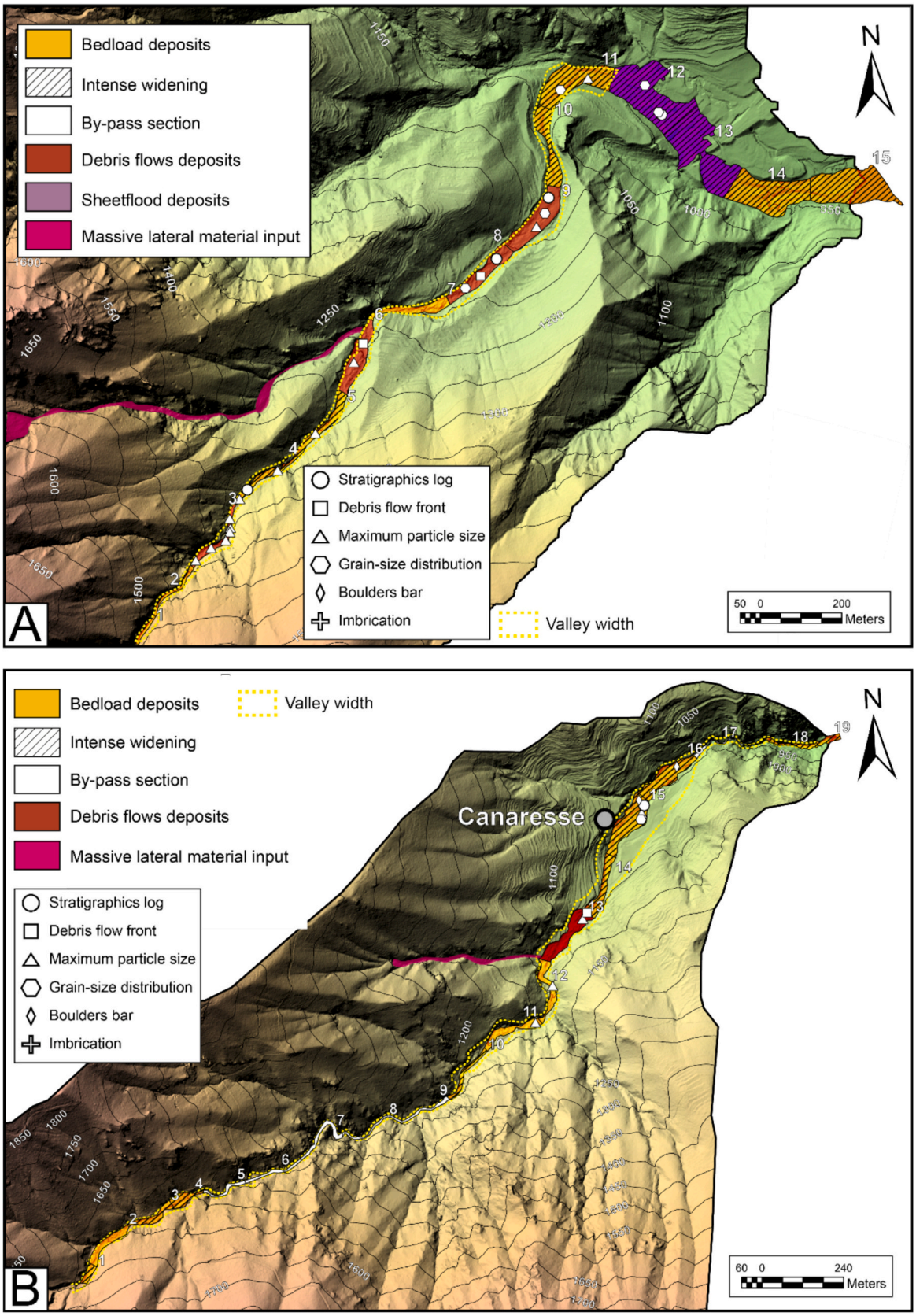

Fig. 10. End-member flow maps of deposits identified during the field survey, together with associated geomorphic and sedimentological features such as boulder bars, grain-size distribution measurements (see Table 3), and locations of stratigraphic logs. Section numbers correspond to those shown in Fig. 9. (A) Dente torrent, (B) Consciente torrent.

Between Sections 12 and 16 (Ci = 5.3), the slope decreases to ~24% in the lower valley near the hamlet of Canaresse, where the channel flows through Triassic cargneules and scree deposits (Fig. 9B). This reach is partially channelised and had an average width of 4.5 m before the flood. Sections 17–18 correspond to a second narrow gorge incised into migmatites (Ci = 2.7, slope ~ 22%) leading to the confluence with the Roya River, where the channel is ~4 m wide.

Following the flood, the mean width ratio reaches 4.4 (Figs. 9B and 10B), indicating average widening from 6 m to 19 m. Widening is most pronounced in the upper reaches (Sections 1–4), with ratios up to 6.1 and widths increasing from 6 m to 24 m. In contrast, gorge sections show limited widening (ratio: 1.9, widths: 4–8 m). The widest expansion occurs in the lower valley (Section 13), where slope decreases and the width ratio peaks at 6.7 (from 5 m to 31 m), before narrowing again downstream (width ratio ~ 2.7).

Bed-level variations (Fig. 9B) reveal a general incision trend (~ − 1 m to ~ − 5 m) in Sections 1–12, with the deepest incision (~ − 5 m) observed in the migmatite gorges (Section 6). Although quantitative data are lacking for Sections 12–18, field observations indicate aggradation where slopes decrease (Sections 12–16). A massive lateral sediment input is observed on the left bank in Section 13, due to landsliding.

The dominant lithofacies are R2 and R3, forming several-metre-thick boulder-bars in low-slope areas near the main channel (Fig. 10B). Aerial imagery shows no deposition within the gorge segments, suggesting bypass flow conditions during the flood. One occurrence of R1 deposits – forming a boulder lobe and frontal accumulation – is observed in Sections 3 (Fig. 9B), near the confluence with landslide-derived debris.

4.2.3. Cairos River

The Cairos River was divided into 33 Sections (Fig. 9C), from Section 1 located upstream to Section 33 at the confluence with the Roya River. The average longitudinal slope is 7% and the mean confinement index is 9.3.

The river flows through a relict glacial valley filled with Würmian terraces (Julian, 1977), bordered by Jurassic limestone and dolomite cliffs (Figs. 2B and 9CC). Two main segments can be distinguished. The upper reach (Sections 1–16, Ci = 7) has an average slope of 9% and a pre-flood channel width of ~9 m. The lower reach (Sections 17–33, Ci = 11) displays gentler slopes (~6%) and a pre-flood channel width of ~7 m. The transition between both corresponds to a narrow gorge (Sections 12–16) incised into limestones (Ci = 5.1, slope of ~9%, Fig. 9C).

After the flood, the average width ratio was 3.3, increasing from ~8 m to ~27 m (Fig. 9C). The upper reach shows a mean width ratio of ~2.6 (post-flood width ~ 21 m), whereas the lower reach nearly doubles this value, with a ratio of ~4.1, and widths up to ~32 m. Even the gorge section widened significantly (ratio 2.5, max width 21 m), occupying the entire gorge cross-section.

Bed-level changes (Fig. 9C) indicate a general incision trend in the upper reach (Sections 1–18) ranging from ~ − 1 m to ~ − 2 m. The lower reach shows localised aggradation in Sections 20, 26, 29, and 31, with values between +0.5 to +1.5 m. However, field observations suggest significant aggradation across the valley floor, with overbank and marginal deposits compensating for inner-channel incision (Figs. 8C and 11).

The dominant lithofacies are R2, S1, and S2, corresponding respectively to boulder bars, cobble–pebble deposits and overbank facies (Fig. 11). Boulder fronts and lobes corresponding to R1 facies are found in Sections 5–6, 22, 26, and 30 (see supplementary material 1). These areas correspond to tributary confluences or bank failures, mostly along the right bank (Fig. 11). In these sectors, slopes range between 6% and 8%, and the average width ratio is 4, with channel widening from 17 to 45 m post-flood.

5. Discussions

This section explores the spatial distribution of sedimentary deposits within the Dente, Consciente, and Cairos catchments, with a focus on both lateral and longitudinal variability where field conditions allow. The Dente and Consciente torrents, characterised by their steep longitudinal gradients, exhibit well-defined lateral and vertical facies variations. In the Dente torrent, a combination of laminar and turbulent flow was documented (based on flow end-member deposits, e.g. R1, R2, R3,

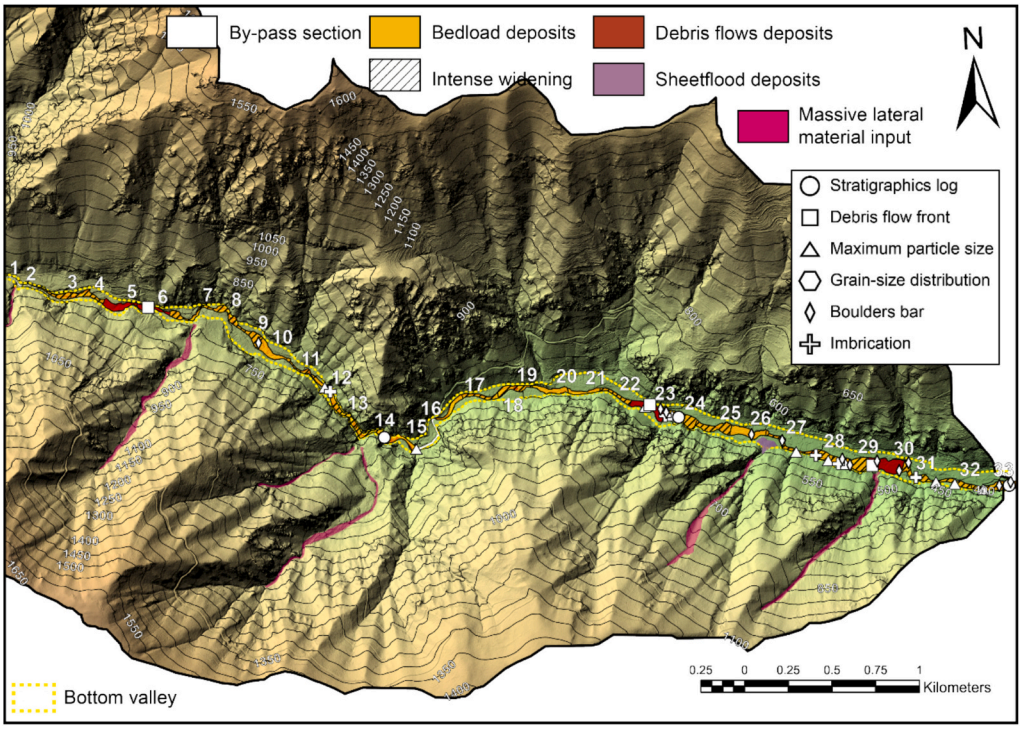

Fig. 11. End-member flow map of deposits identified during the field survey along the Cairos river. Associated geomorphic and sedimentological features, such as boulder bars, grain-size distribution measurements, and the locations of stratigraphic logs, are also shown. Section numbers correspond to those presented in Fig. 9.

R4), whereas in the Consciente and Cairos rivers, bedload-dominated facies (R2, R3) are more prevalent. In the latter systems, debris-flow deposits (R1) are confined to localised zones, typically in association with significant sediment inputs from hillslope failures or mass-wasting events. This observed facies variability likely reflects a complex interplay between morphometric parameters (e.g. slope, channel confinement), the lithological diversity of each catchment, and dominant sediment transport processes during the flood event.

5.1. Morphometric controls

Slope and channel width exert a first-order control on the type and distribution of sedimentary deposits (Benda, 1990; Iverson, 1997; Moscariello et al., 2002; Takahashi, 2014; Tjalling De Haas et al., 2016). Debris-flow facies (R1) are typically localised at slope breaks or areas of slope decrease as observed in the Dente torrent (Figs. 9, 10 and 11), where end-member deposits occur in sharply reduced slope segments compared to adjacent reaches.

Channel width is another key morphometric factor influencing depositional style (Jin et al., 2022). In both the Dente and Consciente torrents, debris-flow features such as levees, boulder fronts, or lobe-shaped accumulations are found in the widest channel reaches (Fig. 10) for instance, in Dente, Sections 7–8 show post-flood widths ranging from 14 to 28 m (width ratio = 2–5.2), while in Consciente, Sections 10–11 span 22–37 m (width ratio = 2.7–4.8). These patterns are consistent with high confinement index values observed in areas of debris-flow deposition.

The Cairos differs significantly from the other in terms of size, slope, lithology, and rainfall. It is dominated by bedload and suspended sediment transport, with sandy overbank and boulder-bar deposits typical of debris floods (Brenna et al., 2023; Brenna et al., 2020; Church and Jakob, 2020). At several right-bank confluences (Sections 23, 26 and 30), debris-flow fronts are associated with strong local channel widening (width ratio > 4.5). For example, in Section 23, the width ratio increases from 2 to 8 and remains >2 from Sections 23 to 30. This agrees with Brenna et al. (2023), who showed that debris-flow pulses from tributaries progressively dilute downstream into type II debris floods (Church and Jakob, 2020), promoting localised channel widening (Fig. 11).

Additional sediment inputs occurred at Sections 1, 15, and 16, but we suggest that the resulting deposits were not preserved due to steep slopes ($> 9\%$) and narrow channel confinement (Fig. 11). Conversely, at Sections 5–6, large debris-flow lobes result from bank collapse along terraces up to 10 m high, compared to <3 m further downstream. Overall, tributary-derived debris-flow were rapidly diluted and preserved only where valley width increased and slope decreased.

In contrast, constricted channel sectors often correspond to by-pass zones or areas of local flow blockage that strongly influence sediment retention and deposit geometry. In Dente, Section 7 forms a gorge reach flanked by debris-flow deposits (Fig. 10A). A similar constriction occurs in Consciente at the start of section 13 (Fig. 10B), and in Cairos at Sections 5–6 (Fig. 11). These narrow segments, especially when combined with large sediment inputs and temporary log-jams caused by riparian erosion (Martini et al., 2025; Piton et al., 2024), likely promoted debris-flow deposition and limited runout distances (Booth et al., 2020).

These findings align with the observed relationship between channel widening and the Confinement Index (Ruiz-Villanueva et al., 2023 and references therein). For example, in the Dente torrent, the downstream reach just upstream of the alluvial fan apex is unconfined (Fig. 9), in agreement with field observations (Fig. 10A). Sections 8–9 contain both surface and subsurface evidence of debris-flow fronts. In the Cairos River, a clear relationship is also observed between the Confinement Index and the Width Ratio, illustrating progressive channel widening from the headwaters to the lower catchment (Fig. 9C).

5.2. Role of fine-grained particles in flow rheology

The Dente torrent is characterised by abundant lithofacies R1, interpreted as debris-flow deposits, interbedded with R2-R3 or R2-R4 layers representing bedload and suspended or hyperconcentrated flow deposits (Table 3). It is the only torrent showing numerous debris-flow horizons alternating with turbulent bedload units (Figs. 4–6). These vertical variations reflect fluctuating flow conditions during the event, expressed as sediment-pulse sequences (Hungr et al., 2014) caused by lateral inputs such as landslides, bank erosion (Cruden and Varnes, 1996; Hungr et al., 2014; Watters and Robert, 1983) or remobilization of in-channel material (Baggio et al., 2024). Well-developed clast imbrication and alignment in R2 suggest “intersurge” phases (Nemec and Steel, 1984), when flow temporarily became more diluted and allowing bedload transport.

On the Vievola fan, the vertical succession R3–R4–R2–R1 (Fig. 5) reflects spatial and temporal variations in flow energy and sediment load. R4 (sheet-flood, Fig. 4) deposits formed under supercritical flow in unconfined zones (Blair, 1987, 2000), whereas central areas record hyperconcentrated (R3) and debris-flow (R1) phases locally influenced by the presence of the railway bridge. Downstream, the progressive fining and reduction in cohesion indicate a decline in flow energy as the flood spread across the fan.

Compared with the Consciente torrent, where transport is dominated by bedload (Fig. 7), the Dente torrent exhibits a higher proportion of debris-flow deposits (Fig. 4). This difference can be linked to the greater availability of fine-grained particles, which enhance the viscous and buoyant behaviour of the flow (Costa, 1984; Iverson, 2014; Iverson, 1997; Jakob and Hungr, 2005; Major and Pierson, 1992). On average, R1 deposits in Dente torrent contain about +5 wt% more fines than other lithofacies (Table 3). Although clay content remains low (0.3–0.7 wt%), the silt fraction increases markedly (+1.3–5.7 wt%). Numerous studies emphasise the critical role of clay and silt in controlling debris-flow rheology (Bolliger et al., 2024; Chen et al., 2022; De Haas et al., 2015; Hürlimann et al., 2015; Kostynick et al., 2022; Moscariello et al., 2002). Small increases in clay content can enhance runout distance and velocity (Iverson et al., 2010), whereas excessive clay tends to increase viscosity, potentially reducing both parameters (Iverson, 1997).

In contrast, the Cairos River shows low clay contents (between 0.06 and 0.15 wt%) and low silts fractions (0.8–1.9 wt%) compared with the two others catchments (Table 3). Its deposits are dominated by gravel and sand (22–48 wt% and 50–82 wt% respectively) which correspond more closely to the properties of debris flood behaviour (Brenna et al., 2020; Church and Jakob, 2020).

5.3. Lithological control on sediment production

Dente and Consciente torrents share similar morphometric characteristics (Table 2, Fig. 2A and B), including catchment area, mean channel slope, and hillslope gradient. Their main difference lies in lithology:

- Dente torrent: ~46% scree and fluvioglacial deposits, 48% limestone and dolomite lithologies.
- Consciente torrent: ~77% limestone/migmatite, 20% scree, and 3% others lithologies.

Grain-size data indicate a higher fine fraction (mainly silt) in Dente, whereas Consciente is dominated by coarser, pebbles- and sand-rich material. The abundance of fines in Dente is attributed to the presence of scree and fluvioglacial deposits (Table 2, Fig. 2), which supplied large volumes of sediments through gully flushing and bank erosion during Storm Alex. These lithologies promote fine-particle generation and favour debris-flow development (Moscariello et al., 2002; Remaître et al., 2011) when sufficient water supply, slope, and sediment availability are combined (Iverson, 1997). In contrast, Consciente shows only a single debris-flow event, likely linked to shallow landsliding that enriched the flow matrix in fines. The upper Consciente catchment

(Fig. 2B), composed mainly of anatexites, favours sandy deposits, while the downstream widening near Canaresse corresponds to scree-dominated reaches with sandier facies (Fig. 7). The Cairos River shows grain-size distribution comparable to the Consciente torrent (Table 3). In this case, most left-bank tributaries contributed substantial sediment inputs to the main channel, despite lower rainfall than in the northern sectors (Fig. 11). Notably, the most active tributaries are located in Cretaceous marls and marl–limestones (Figs.2 and 11), lithologies that exhibit high erodibility and sediment yield (Remaître, 2006; Remaître et al., 2005).

In both Dente and Consciente, major post-flood channel widening (Fig. 9) occurred primarily within unconsolidated lithologies (scree and fluvioglacial deposits), with average width ratios of ~6, compared to 3.7 in limestone–dolomite and ~ 1.8 in migmatite zones. Resistant bedrock promoted vertical incision rather than lateral expansion. Beyond fine content, the total sediment volume incorporated into the flow is also critical for debris-flow magnitude (Jakob, 2005; Morel et al., 2023; Rickenmann, 1999). When sediment availability is limited, even high-energy flows tend to transition into bedload-dominated transport or type II debris floods (Church and Jakob, 2020).

The dense vegetation cover in Dente torrent and Cairos River (Piton et al., 2024), combined with large sediment inputs from gullies and bank erosion (> 30,000 m^3), and the abundance of fine-grained material derived from fluvioglacial deposits (Dente), likely favored the development of debris-flow pulses.

In glacial valleys such as Cairos, alluvial terraces act as sediment sources through bank erosion (Liébault et al., 2024). Channel widening - and therefore width ratios - are partly governed by slope and confinement (Ruiz-Villanueva et al., 2023 and references therein). Overall, grain-size distribution and the presence of erodible lithologies (e.g., fluvioglacial outwash, marls) exert a strong control on sediment transport dynamics and the incorporation of fine material into the flow.

5.4. Controls on facies associations

The material deposited into the channel is progressively reworked and transported downstream through stepwise motion. These dynamics correspond to autogenic fluvial processes (Jerolmack and Paola, 2010; Paola, 2016), characterised by scour-and-fill sequences that facilitate mass displacement along the channel. Such movements are driven by bedload transport, forming migrating bedload sheets (Recking et al., 2009) as well as lateral and longitudinal bars (Miall, 2014, 2022; Miall, 1996). An example of the initiation and deposition of a bedload sheet is observed in the Vievola catchment within facies R2 (Fig. 5). During high-discharge events, the high sediment load promotes rapid particle mobilisation and the development of such sedimentary structures. Vertical lithofacies reflect this variation and explain the normal graded to inverse grading interpretation of R2 to R4 lithofacies in all different catchments.

The intense bedload transport observed during Storm Alex can be interpreted as a phase of highly efficient bedload motion (Carling, 1987; Frey and Church, 2011; Frey and Church, 2009) approaching the debris flood regime (Church and Jakob, 2020). This transport corresponds to a dense, near-continuous bedload layer (Frey and Church, 2011) involving large-scale mobilisation of the streambed over several hundred metres. Such movement produces characteristic sedimentary structures generated by kinetic sorting, a grain-to-grain segregation mechanism combining kinetic sieving and squeeze expulsion (Gray and Thornton, 2005; Gray, 2018), which induces an efficient downward migration of fine particles and upward displacement of coarser ones called “kinetic sorting” (Bacchi et al., 2014; Dudill et al., 2017; Recking et al., 2009). This process results in inverse or locally ungraded structures, typical of bedload-sheet transport, where the entire bed surface behaves as a mobile granular layer.

As highlighted by Bacchi et al. (2014), during their experiments, temporary bed armouring develops as fine particles infiltrate the lower part of the bedload layer, reducing entrainment from the substrate. However, this subsurface enrichment in fines also promotes instability: once the local slope reaches a critical value, the armour layer collapses, leading to sudden erosion and downstream propagation of bedload sheets (Recking et al., 2009). These alternations of aggradation and erosion reflect cyclic fluctuations of slope and sediment-transport efficiency (and thus solid discharge), driven by internal bed reorganisation rather than by variations in discharge (Bacchi et al., 2014) and do not necessarily involve new sedimentary input.

Such cycles explain the formation of sandy horizons within coarse deposits observed in the Cairos River and on the Vievola fan. These layers likely correspond to transient stages of fine accumulation produced by kinetic sorting during bedload-sheet migration and local slope adjustments.

5.5. Implications and synthesis of flow dynamics during an extreme event

This study complements and extends recent work by Brenna et al. (2020, 2023) on the types of flow generated during extreme events and their longitudinal and vertical successions. These observations help to better constrain flow dynamics within a single catchment, considering both large sediment supply and autogenic processes.

Fig. 12 illustrates how sedimentary facies and deposits reflect geomorphological responses to such extreme events, driven by rainfall intensity, morphometric parameters, and lithological control. It presents synthetic facies for four end-member scenarios following an extreme hydro-sedimentary event, showing how these parameters, along with the volume of eroded material, influence the development of distinct flow types (bedload, hyperconcentrated flow, debris flow).

Integrating geomorphological and sedimentological perspectives thus refines our understanding processes of extreme events, emphasising site-specific controls within each activated catchment. Identifying source areas (including glacial and fluvio-glacial deposits) and evaluating their connectivity to the main channel enable a more accurate assessment of flood and debris flow hazards, whether dominated by clear water flow, bedload transport, hyperconcentrated flow or debris flow. Moreover, recognising past events preserved in the sedimentary record, when available, may provide insights into the recurence, magnitude and thresholds of similarly extreme episodes, contributing to a long-term hazard reconstruction and mitigation strategies.

6. Limitations and perspectives

This raises further questions: how are deposits linked to extreme events preserved through time? Are they rapidly reworked (Joyce et al., 2018; Milan, 2012; Pitlick, 1993) over short geological timescales, such as during the Holocene? In what form are these deposits recorded within ancient sedimentary basins, and how can they be integrated into source-to-sink budgets (Romans et al., 2016; Straub et al., 2020; Tofelde et al., 2021).

It raises major questions for paleohydraulic reconstructions (Benito et al., 2022) and for improving flood-frequency analyses. The chaotic nature of these processes induces rapid alternations of erosion, transport, and deposition phases, resulting in the formation of multiple sedimentary sequences - even though all of them may originate from a single extreme storm event occurring within a single day. Without a careful spatial and temporal framework, this diversity of deposits could be misinterpreted as a succession of unrelated strata.

Another major question concerns whether paleo–debris flood deposits (Brenna et al., 2024) can be identified within ancient alluvial terraces, allowing the recognition of past periods of intense bedload transport linked to discrete events, or whether their sedimentary signal has been progressively shredded and dispersed through time?

The main limitations of this study lie in the fact that the analysed deposits represent only the preserved end-member facies that remained after deposition. The complete sequence of flow events preceding these

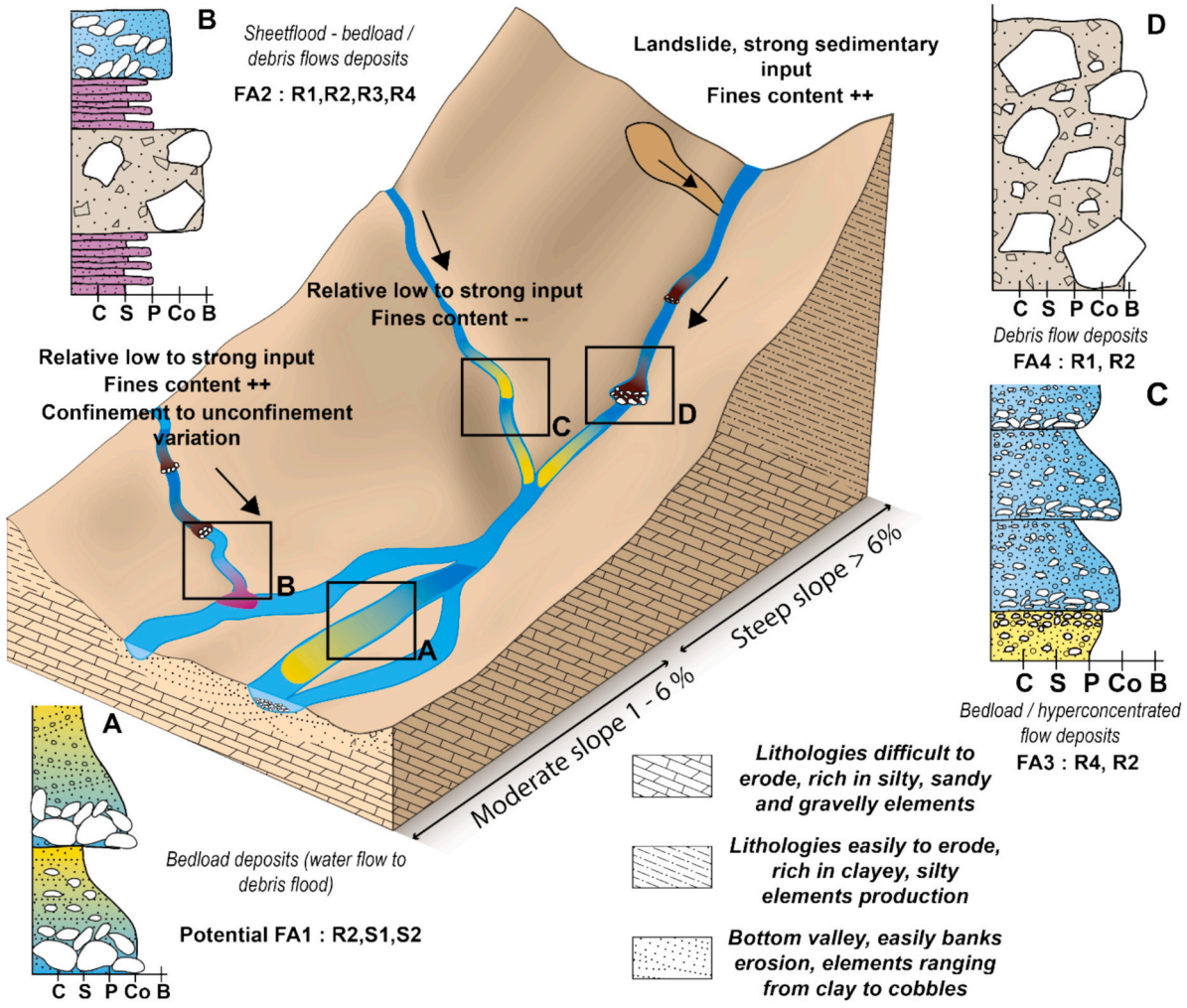

Fig. 12. Synthetic logs illustrating the main end-members flow types following an extreme hydro-sedimentary event in mountainous terrain, based on observations from Storm Alex and the associated sedimentary facies. Four main facies association (FA) are distinguished: i) FA1 (R2, S1, S2) – Fully turbulent flows, occurring in sectors with slopes between < 1% and ~ 6% ii), FA2 (R1, R2, R3, R4) – Alternation between channelised and unconfined flows, with laminar-to-turbulent transport associated with a progressive decrease in slope. iii) FA3 (R4, R2) – Steep torrents with moderate-to -high sediment supply but low fine content, favouring turbulent transport associated with occasional pulses of laminar flow. iv) FA4 (R1, R2) – Steep torrents (slope > 6%) with high sediment supply and abundant fines, promoting laminar flow with episodic surges of turbulent transport during inter-surge phases.

deposits may not have been fully recorded, and some facies associations might be missing or remain undescribed. Furthermore, extensive post-flood reworking within the Roya River channel has prevented a clear identification of its own depositional dynamics during Storm Alex.

Another limitation of this study is the absence of detailed hydraulic data – such as stream power estimates per section – which would allow a more robust assessment of the link between flow energy, lateral erosion, and sedimentary patterns.

From a hazard-management perspective, these results stress the need for integrated mapping and susceptibility assessments in steep mountainous valleys, where multiple flow processes may coexist during a single event. Moreover, our multi-scale framework can inform more effective land-use planning and infrastructural design. Looking ahead, the increasing likelihood of extreme rainfall under ongoing climate change suggests such hazardous events may become more frequent, reinforcing the urgency of proactive risk-mitigation strategies.

7. Conclusions

In this study, we analysed deposits formed during Storm Alex (2 October 2020) in the Roya Valley, exploring multiple sub-catchments to elucidate flow processes responsible for the observed lithofacies. Our main indicate two primary drivers of flow generation: (1) morphometric factors (slope, confinement, width ratio), which control flow depth and channel expansion, and (2) fine-grained sediment, which influences cohesion and flow rheology. These parameters depend on the lithology encountered and the volume of eroded material made available during the event, and the contribution of large wood mobilised by lateral bank erosion which can significantly influence flow dynamics and sediment deposition.

We underline the crucial role of lithology in both flow generation and sediment sourcing. Because of its glacial inheritance and lithological composition, the Dente torrent is more prone to debris-flow activity, whereas the Consciente torrent and the Cairos River are dominated by intense bedload transport typical of debris floods. In these systems, debris-flow deposits occur only at confluences receiving significant lateral inputs. The gradual widening of the Cairos River reflects sedimentary cascades triggered by large lateral contributions eroding the Würmian terraces.

High width ratios (Wr > 4) correspond to the sectors most affected by intense rainfall, illustrating the exceptional magnitude of Storm Alex. Moreover, the relationship between key morphometric parameters – such as the confinement index, width ratio, and, to a first order, the slope – shows a consistent spatial pattern that aligns closely with the

distribution of the observed end-member deposits. These findings build upon previous research by demonstrating how a single extreme rainfall event can generate highly variable sedimentary signatures across adjacent catchments. Such disparities underline how a single extreme rainfall episode (with a > 1000-year return period) challenges the interpretation of fossil deposits in the geological record when precise temporal constraints are lacking.

Ultimately, our observations emphasise the complexity of flow transitions (from debris flows to bedload transport) and the combined influence of topographic and lithological constraints. This high-resolution documentation of Storm Alex deposits provides a valuable reference case for the study of extreme hydro-sedimentary events, highlighting the importance of multi-scale and interdisciplinary approaches (geomorphology, sedimentology, hydrology) in mountainous environments.

CRediT authorship contribution statement

Raphaël Kerverdo: Writing – review & editing, Writing – original draft, Visualization, Supervision, Methodology, Investigation, Funding acquisition, Formal analysis, Data curation, Conceptualization. **S. Lafuerza:** Writing – review & editing, Visualization, Validation, Supervision, Software, Investigation, Funding acquisition, Conceptualization. **C. Gorini:** Writing – review & editing, Visualization, Validation, Supervision, Funding acquisition. **E. Fouache:** Visualization, Validation, Supervision. **D. Granjeon:** Writing – review & editing, Visualization, Validation, Methodology, Conceptualization. **R. Deschamps:** Writing – review & editing. **S. Migeon:** Writing – review & editing, Visualization, Validation. **J.L. Rubino:** Investigation. **P.Y. Lagrée:** Investigation. **M. Jafari:** Investigation. **N. Bianchi:** Investigation.

Declaration of competing interest

The authors declare that they have no known competing financial interests or personal relationships that could have appeared to influence the work reported in this paper.

Acknowledgements

The authors would like to express their sincere gratitude to the two anonymous reviewers for the time they devoted to this manuscript and for all their comments, which greatly improved its quality. This research was supported by the *Terre–Mer* team of the UMR 7193 – Institut des Sciences de la Terre de Paris (ISTeP), Sorbonne Université, CNRS and by a doctoral fellowship from the French Ministry of Research. Additional funding was provided by the CNRS through the MITI programme for field equipment, and by the *Institut Jean le Rond d'Alembert* for the final field campaign. *The Institute of Ocean* and the *Institute of Environmental Transition* (Alliance Sorbonne University) also supported three field missions. The authors thank the *Monastery of Saorge (Centre des Monuments Nationaux)* for providing accommodation during fieldwork. Finally, We would like to thank G. Piton (INRAE) for his valuable advice and constructive recommendations, which greatly helped to improve the quality of this article.

Appendix A. Supplementary data

Supplementary data to this article can be found online at https://doi.org/10.1016/j.catena.2026.110054.

References

Alber, A., Piégay, H., 2011. Spatial disaggregation and aggregation procedures for characterizing fluvial features at the network-scale: application to the rhône basin (France). Geomorphology 125, 343–360. https://doi.org/10.1016/j.geomorph.2010.09.009.

Allen, J.R.L., 1982. Sedimentary Structures, their Character and Physical Basis, Developments in Sedimentology. Elsevier Scientific Pub. Co, Amsterdam; New York.

Ashley, G.M., 1990. Classification of large-scale subaqueous bedforms: a new look at an old problem. Journal of Sedimentary Petology 60, 160–172.

Bacchi, V., Recking, A., Eckert, N., Frey, P., Piton, G., Naaim, M., 2014. The effects of kinetic sorting on sediment mobility on steep slopes. Earth Surf. Process. Landf. 39, 1075–1086. https://doi.org/10.1002/esp.3564.

Baggio, T., Martini, M., Bettella, F., D'Agostino, V., 2024. Debris flow and debris flood hazard assessment in mountain catchments. CATENA 245, 108338. https://doi.org/10.1016/j.catena.2024.108338.

Barrier, P., Montenat, C., De Lumley, H., 2009. Empreintes de pas de reptiles au pic des merveilles dans le permien du massif du Mont-Bego (Alpes-Maritimes). Comptes Rendus Palevol 8, 67–78. https://doi.org/10.1016/j.crpv.2008.11.001.

Benda, L., 1990. The influence of debris flows on channels and valley floors in the Oregon coast range, U.S.a. Earth Surf. Process. Landf. 15, 457–466. https://doi.org/10.1002/esp.3290150508.

Benito, G., Harden, T.M., O'Connor, J., 2022. Quantitative Paleoflood Hydrology. In: Treatise on Geomorphology. Elsevier, pp. 743–764. https://doi.org/10.1016/B978-0-12-409548-9.12495-9.

Bigot-Cormier, F., 2002. La surrection du massif cristallin externe de l'Argentera (France-Italie) et ses relations avec la déformation pliocène de la marge Nord-Ligure: Arguments thermochronologiques (traces de fission), géomorphologiques et interprétations de sismique marine.

Blair, T., 1987. Sedimentary processes, vertical stratification sequences, and geomorphology of the Roaring River alluvial fan, Rocky Mountain National Park, Colorado. SEPM JSR 57. https://doi.org/10.1306/212F8A8A-2B24-11D7-8648000102C1865D.

Blair, T., McPherson, J.G., 1994. Alluvial fans and their natural distinction from rivers based on morphology, hydraulic processes, sedimentary processes, and facies assemblages. SEPM JSR 64A. https://doi.org/10.1306/D4267DDE-2B26-11D7-8648000102C1865D.

Blair, T.C., 2000. Sedimentology and progressive tectonic unconformities of the sheetflood-dominated hells gate alluvial fan, death valley, California. Sediment. Geol. 132, 233–262. https://doi.org/10.1016/S0037-0738(00)00010-5.

Blott, S.J., Pye, K., 2001. GRADISTAT: a grain size distribution and statistics package for the analysis of unconsolidated sediments. Earth Surf. Process. Landf. 26, 1237–1248. https://doi.org/10.1002/esp.261.

Bolliger, D., Schlunegger, F., McArdell, B.W., 2024. Comparison of debris flow observations, including fine-sediment grain size and composition and runout model results, at illgraben, swiss alps. Nat. Hazards Earth Syst. Sci. 24, 1035–1049. https://doi.org/10.5194/nhess-24-1035-2024.

Booth, A.M., Sifford, C., Vascik, B., Siebert, C., Buma, B., 2020. Large wood inhibits debris flow runout in forested Southeast Alaska. Earth Surf. Process. Landf. 45, 1555–1568. https://doi.org/10.1002/esp.4830.

Brenna, A., Surian, N., Ghinassi, M., Marchi, L., 2020. Sediment–water flows in mountain streams: recognition and classification based on field evidence. Geomorphology 371, 107413. https://doi.org/10.1016/j.geomorph.2020.107413.

Brenna, A., Marchi, L., Borga, M., Zaramella, M., Surian, N., 2023. What drives major channel widening in mountain rivers during floods? The role of debris floods during a high-magnitude event. Geomorphology 430, 108650. https://doi.org/10.1016/j.geomorph.2023.108650.

Brenna, A., Martini, I., Menapace, L., Surian, N., Ventra, D., Ghinassi, M., 2024. Imbrication fabric as a diagnostic feature for the genetic classification of gravels deposited by fluid-gravity versus sediment-gravity subaerial flows. Earth Surf. Process. Landf. 49, 4088–4098. https://doi.org/10.1002/esp.5986.

Carling, P., 1987. The concept of dominant discharge applied to two gravel-bed streams in relation to channel stability thresholds. Earth Surf. Process. Landf. 13, 355–367.

Carrega, P., Michelot, N., 2021. Une catastrophe hors norme d'origine météorologique le 2 octobre 2020 dans les montagnes des Alpes-Maritimes. Physio-geo 1–70. https://doi.org/10.4000/physio-geo.12370.

Cerema, 2021. RETEX technique ALEX - Inondations des 2 et 3 octobre 2023. consensus hydrologique - Unpublished report - CEREMA.

Chen, T.-Y.K., Hung, C.-Y., Mullenbach, J., Hill, K., 2022. Influence of fine particle content in debris flows on alluvial fan morphology. Sci. Rep. 12, 21730. https://doi.org/10.1038/s41598-022-24397-x.

Church, M., Jakob, M., 2020. What is a debris flood? Water Resour. Res. 56. https://doi.org/10.1029/2020WR027144.

Comiti, F., Lucía, A., Rickenmann, D., 2016. Large wood recruitment and transport during large floods: a review. Geomorphology 269, 23–39. https://doi.org/10.1016/j.geomorph.2016.06.016.

Comiti, F., Righini, M., Nardi, L., Lucía, A., Amponsah, W., Cavalli, M., Surian, N., Marchi, L., Rinaldi, M., Borga, M., 2016b. Channel widening during extreme floods: how to integrate it within river corridor planning? Presented at the 13th congress interpraevent 2016. Lucerne (Switzerland) 477–486.

Costa, J.E., 1984. Physical geomorphology of debris flows. In: Costa, J.E., Fleisher, P.J. (Eds.), Developments and Applications of Geomorphology. Springer Berlin Heidelberg, Berlin, Heidelberg, pp. 268–317. https://doi.org/10.1007/978-3-642-69759-3_9.

Coussot, P., Meunier, M., 1996. Recognition, classification and mechanical description of debris flows. Earth Sci. Rev. 40, 209–227. https://doi.org/10.1016/0012-8252(95)00065-8.

Cronin, S.J., Neall, V.E., Lecointre, J.A., Palmer, A.S., 1999. Dynamic interactions between lahars and stream flow: a case study from ruapehu volcano, New Zealand. Geol. Soc. Am. Bull. 111, 28–38. https://doi.org/10.1130/0016-7606(1999)111<0028:DIBLAS>2.3.CO;2.

Cruden, D.M., Varnes, D.J., 1996. Landslide types and processes. Turner, a.K. And shuster, R.L., eds., landslides: investigation and mitigation, transportation research board special report, 36–75.
De Haas, T., Braat, L., Leuven, J.R.F.W., Lokhorst, I.R., Kleinhans, M.G., 2015. Effects of debris flow composition on runout, depositional mechanisms, and deposit morphology in laboratory experiments. JGR Earth Surface 120, 1949–1972. https://doi.org/10.1002/2015JF003525.
Dudill, A., Frey, P., Church, M., 2017. Infiltration of fine sediment into a coarse mobile bed: a phenomenological study. Earth Surf. Process. Landf. 42, 1171–1185. https://doi.org/10.1002/esp.4080.
Faure-Muret, A., 1955. Etudes géologiques sur le massif de l'Argentera-Mercantour et ses enveloppes sédimentaires.
Frey, P., Church, M., 2009. How river beds move. Science 325, 1509–1510. https://doi.org/10.1126/science.1178516.
Frey, P., Church, M., 2011. Bedload: a granular phenomenon. Earth Surf. Process. Landf. 36, 58–69. https://doi.org/10.1002/esp.2103.
Gèze, B., Nesteroff, N., 1996. Carte géologique de la France à 1/50 000. Feuille: 973 - Menton - Nice. Editions du BRGM, Orléans.
Gray, J.m.n. t, Thornton, A. r, 2005. A theory for particle size segregation in shallow granular free-surface flows. Proc. R. Soc. Lond. A Math. Phys. Eng. Sci. 461, 1447–1473. https://doi.org/10.1098/rspa.2004.1420.
Gray, J.M.N.T., 2018. Particle segregation in dense granular flows. Annu. Rev. Fluid Mech. 50, 407–433. https://doi.org/10.1146/annurev-fluid-122316-045201.
Hampton, M.A., 1979. Buoyancy in debris flows. J. Sedimentary Pretology 49, 753–758.
Hugerot, T., Astrade, L., Gauchon, C., 2024. Trajectoires paysagères et crises morphosédimentaires de cônes torrentiels dans la vallée de la maurienne (savoie) depuis la fin du petit âge glaciaire: Études géohistoriques à travers les dynamiques doccupation des sols. Paysage 30. https://doi.org/10.4000/120t1.
Hungr, O., Morgan, G.C., Kellerhals, R., 1984. Quantitative analysis of debris torrent hazards for design of remedial measures. Can. Geotech. J. 21, 663–677. https://doi.org/10.1139/t84-073.
Hungr, O., Evans, S.G., Bovis, M.J., Hutchinson, J.N., 2001. A review of the classification of landslides of the flow type. Environ. Eng. Geosci. 7, 221–238. https://doi.org/10.2113/gseegeosci.7.3.221.
Hungr, O., Leroueil, S., Picarelli, L., 2014. The varnes classification of landslide types, an update. Landslides 11, 167–194. https://doi.org/10.1007/s10346-013-0436-y.
Hürlimann, M., McArdell, B.W., Rickli, C., 2015. Field and laboratory analysis of the runout characteristics of hillslope debris flows in Switzerland. Geomorphology 232, 20–32. https://doi.org/10.1016/j.geomorph.2014.11.030.
IGN, 2020. Un avion de l'IGN photographie les zones sinistrées [WWW Document]. un avion de l'IGN photographie les zones sinistrées. https://www.ign.fr/institut/nos-domaines-dintervention/prevention-des-risques/tempete-alex-un-avion-de-lign-photographie-les-zones-sinistrees.
IGN, 2023a. LiDAR HD Version 1.0 - Descriptif de contenu des nuages de points LiDAR. In: Institut National de l'Information Géographique et Forêstière, Paris.
IGN, 2023b. MNS Correl Version 1.0 - Descriptif de contenu. In: Institut National de l'Information Géographique et Forêstière, Paris.
Iverson, R.M., 1997. The physics of debris flows. Rev. Geophys. 35, 245–296. https://doi.org/10.1029/97RG00426.
Iverson, R.M., 2014. Debris flows: behaviour and hazard assessment. Geol. Today 30, 15–20. https://doi.org/10.1111/gto.12037.
Iverson, R.M., Logan, M., LaHusen, R.G., Berti, M., 2010. The perfect debris flow? Aggregated results from 28 large-scale experiments. J. Geophys. Res. 115, 1–29. https://doi.org/10.1029/2009JF001514.
J., Watters Robert, 1983. A landslide induced waterflood-debris flow. Bull. Int. Assoc. Eng. Geol. 28, 177–182. https://doi.org/10.1007/BF02594812.
Jakob, M., 2005. A size classification for debris flows. Eng. Geol. 79, 151–161. https://doi.org/10.1016/j.enggeo.2005.01.006.
Jakob, M., 2021. Debris-flow hazard assessments: a practitioners view. Environ. Eng. Geosci. 27, 153–166. https://doi.org/10.2113/EEG-D-20-00110.
Jakob, M., Hungr, O., 2005. Debris-flow hazards and related phenomena. In: Springer-Praxis Books in Geophysical Sciences. Springer, Berlin Heidelberg.
Jerolmack, D.J., Paola, C., 2010. Shredding of environmental signals by sediment transport. Geophys. Res. Lett. 37, 2010GL044638. https://doi.org/10.1029/2010GL044638.
Jin, W., Wang, H., Zhang, G., Liu, D., Wang, J., 2022. Channel evolution triggered by large flash flood at an earthquake-affected catchment. Remote Sens. 14, 6060. https://doi.org/10.3390/rs14236060.
Joyce, H.M., Hardy, R.J., Warburton, J., Large, A.R.G., 2018. Sediment continuity through the upland sediment cascade: geomorphic response of an upland river to an extreme flood event. Geomorphology 317, 45–61. https://doi.org/10.1016/j.geomorph.2018.05.002.
Julian, M., 1977. Une carte géomorphologique des alpes maritimes franco-italiennes au 1/200 000e en couleurs. Présentation succincte. Medit 28, 45–53. https://doi.org/10.3406/medit.1977.1709.
Julian, M., 1980. Les Alpes maritimes franco-italiennes: étude géomorphologique. Université de Lille III, Lille.
Kerverdo, R., Lafuerza, S., Gorini, C., Rabaute, A., Granjeon, D., Deschamps, R., Fouache, E., Jafari, M., Lagrée, P., 2025. The impact of storm Alex on the Vievola catch- ment: a quantitative analysis of sediment vol- ume and morphological changes in the Roya river tributaries. Landslides 9. https://doi.org/10.1007/s10346-024-02361-2.
Kostynick, R., Matinpour, H., Pradeep, S., Haber, S., Sauret, A., Meiburg, E., Dunne, T., Arratia, P., Jerolmack, D., 2022. Rheology of debris flow materials is controlled by the distance from jamming. Proc. Natl. Acad. Sci. USA 119, e2209109119. https://doi.org/10.1073/pnas.2209109119.
Krapesch, G., Hauer, C., Habersack, H., 2011. Scale orientated analysis of river width changes due to extreme flood hazards. Nat. Hazards Earth Syst. Sci. 11, 2137–2147. https://doi.org/10.5194/nhess-11-2137-2011.
Lanteaume, M., 1991. Carte géologique de la France à 1/50 000. In: Feuille: 948. BRGM, Orléans, Vièvе-Tende. Editions du.
Liébault, F., Melun, G., Piton, G., Chapuis, M., Passy, P., Tacon, S., 2024. Channel change during catastrophic flood: example of storm alex in the vésubie and roya valleys. Geomorphology 446, 109008. https://doi.org/10.1016/j.geomorph.2023.109008.
Lowe, D.R., 1982. Sediment gravity flows: II. depositionnal models with special reference to the deposits of high-density turbidity currents. J. Sedimentary Pretology 52.
Lucía, A., Schwientek, M., Eberle, J., Zarfl, C., 2018. Planform changes and large wood dynamics in two torrents during a severe flash flood in braunsbach, Germany 2016. Sci. Total Environ. 640–641, 315–326. https://doi.org/10.1016/j.scitotenv.2018.05.186.
Magilligan, F.J., 1992. Thresholds and the spatial variability of flood power during extreme floods. Geomorphology 5, 373–390. https://doi.org/10.1016/0169-555X(92)90014-F.
Major, J.J., Pierson, T.C., 1992. Debris flow rheology: experimental analysis of fine-grained slurries. Water Resour. Res. 28, 841–857. https://doi.org/10.1029/91WR02834.
Manville, V., White, J.D.L., 2003. Incipient granular mass flows at the base of sediment-laden floods, and the roles of flow competence and flow capacity in the deposition of stratified bouldery sands. Sediment. Geol. 155, 157–173. https://doi.org/10.1016/S0037-0738(02)00294-4.
Marchi, L., D'Agostino, V., 2004. Estimation of debris-flow magnitude in the eastern italian alps. Earth Surf. Process. Landf. 29, 207–220. https://doi.org/10.1002/esp.1027.
Martini, M., D'Agostino, V., Piton, G., 2025. Geomorphic activity and related large wood recruitment during debris flows and debris floods: storm alex in the vésubie valley (France). CATENA 257, 109180. https://doi.org/10.1016/j.catena.2025.109180.
Miall, A., 2014. Fluvial Depositional Systems, Springer Geology. Springer International Publishing, Cham. https://doi.org/10.1007/978-3-319-00666-6.
Miall, A.D., 1996. The Geology of Fluvial Deposits, 1st ed. Springer Berlin Heidelberg, Berlin, Heidelberg. https://doi.org/10.1007/978-3-662-03237-4.
Miall, A.D., 2022. Stratigraphy: A Modern Synthesis, Springer Textbooks in Earth Sciences, Geography and Environment. Springer International Publishing, Cham. https://doi.org/10.1007/978-3-030-87536-7.
Middleton, G.V., Hampton, M.A., 1973. Part I. Sediment Gravity Flows: Mechanics of Flow and Deposition.
Milan, D.J., 2012. Geomorphic impact and system recovery following an extreme flood in an upland stream: Thinhope burn, northern England, UK. Geomorphology 138, 319–328. https://doi.org/10.1016/j.geomorph.2011.09.017.
Morel, M., Piton, G., Kuss, D., Evin, G., Le Bouteiller, C., 2023. Statistical modelling of sediment supply in torrent catchments of the Northern French Alps. https://doi.org/10.5194/egusphere-2022-1494.
Moscariello, A., Marchi, L., Maraga, F., Mortara, G., 2002. Alluvial fans in the Italian Alps: Sedimentary facies and processes. In: Martini, I.P., Baker, V.R., Garzón, G. (Eds.), Flood and Megaflood Processes and Deposits. Wiley, pp. 141–166. https://doi.org/10.1002/9781444304299.ch9.
Nemec, W., Steel, R.J., 1984. Alluvial and coastal conglomerates: their significant features and somme comments on gravelly mass-flow deposits. Can. Soc. Petrol. Geol. Mem. 10, 1–31.
ONF-RTM, ONF-DRN, INRAE-ETNA, 2023. Retour dexpérience technique de la crue du 2 octobre 2020 dans la vallée de la roya - volet torrentiel. 10.57745/B69M2O.
Paola, C., 2016. A Mind of their Own: Recent Advances in Autogenic Dynamics in Rivers and Deltas. In: Budd, D.A., Hajek, E.A., Purkis, S.J. (Eds.), Autogenic Dynamics and Self-Organization in Sedimentary Systems. SEPM Society for Sedimentary Geology, p. 0. https://doi.org/10.2110/sepmsp.106.04.
Pierson, T.C., 2005a. Hyperconcentrated flow — Transitional process between water flow and debris flow. In: Debris-Flow Hazards and Related Phenomena, Springer Praxis Books. Springer Berlin Heidelberg, Berlin, Heidelberg, pp. 159–202. https://doi.org/10.1007/3-540-27129-5_8.
Pierson, T.C., 2005b. Distinguishing between Debris Flows and Floods from Field Evidence in Small Watersheds. Fact Sheet.
Pierson, T.C., Costa, J.E., 1987. A rheologic classification of subaerial sediment-water flows. Rev. Eng. Geol. 7, 1–12. https://doi.org/10.1130/REG7-p1.
Pitlick, J., 1993. Response and recovery of a subalpine stream following a catastrophic flood. Geol. Soc. Am. Bull. 105, 657–670.
Piton, G., Cohen, M., Flipo, M., Nowak, M., Chapuis, M., Melun, G., Robert, Y., Andréis, N., Liebault, F., 2024. Large in-stream wood yield during an extreme flood (storm alex, october 2020, roya valley, France): estimating the supply, transport, and deposition using GIS. Geomorphology 446, 108981. https://doi.org/10.1016/j.geomorph.2023.108981.
Pons, A.F., Bonnifait, L., Criado, D., Payrastre, O., Billaud, F., Brigode, P., Fouchier, C., Gourbesville, P., Kuss, D., Le Nouveau, N., Martin, O., Martins, C., Nomis, S., Paquet, E., Cardelli, B., 2024. Consensus hydrologique de la tempête ALEX du 2 et 3 octobre 2020 dans les Alpes-Maritimes. LHB 110, 2363619. https://doi.org/10.1080/27678490.2024.2363619.
Rathburn, S.L., Bennett, G.L., Wohl, E.E., Briles, C., McElroy, B., Sutfin, N., 2017. The fate of sediment, wood, and organic carbon eroded during an extreme flood, Colorado front range, USA. Geology 45, 499–502. https://doi.org/10.1130/G38935.1.
Recking, A., Frey, P., Paquier, A., Belleudy, P., 2009. An experimental investigation of mechanisms involved in bed load sheet production and migration. J. Geophys. Res.: Earth Surf. 114. https://doi.org/10.1029/2008JF000990.

Remaître, A., 2006. Morphologie et dynamique des laves torrentielles: Applications aux torrents des Terres Noires du bassin de Barcelonnette (Alpes du Sud) (Géomorphologie). Université de Caen, Caen.
Remaître, A., Malet, J., Maquaire, O., 2005. Morphology and sedimentology of a complex debris flow in a clay-shale basin. Earth Surf. Process. Landf. 30, 339–348. https://doi.org/10.1002/esp.1161.
Remaître, A., Malet, J.-P., Maquaire, O., 2011. Geomorphology and kinematics of debris flows with high entrainment rates: a case study in the south french alps. Comptes Rendus. Géoscience 343, 777–794. https://doi.org/10.1016/j.crte.2011.09.007.
Rickenmann, D., 1999. Empirical relationships for debris flows. Nat. Hazards 19, 47–77.
Rickenmann, D., Koschni, A., 2010. Sediment loads due to fluvial transport and debris flows during the 2005 flood events in Switzerland. Hydrol. Process. 24, 993–1007. https://doi.org/10.1002/hyp.7536.
Rinaldi, M., Amponsah, W., Benvenuti, M., Borga, M., Comiti, F., Lucía, A., Marchi, L., Nardi, L., Righini, M., Surian, N., 2016. An integrated approach for investigating geomorphic response to extreme events: methodological framework and application to the october 2011 flood in the magra river catchment, Italy: integrated approach for investigating geomorphic response to floods. Earth Surf. Process. Landf. 41, 835–846. https://doi.org/10.1002/esp.3902.
Romans, B.W., Castelltort, S., Covault, J.A., Fildani, A., Walsh, J.P., 2016. Environmental signal propagation in sedimentary systems across timescales. Earth Sci. Rev. 153, 7–29. https://doi.org/10.1016/j.earscirev.2015.07.012.
Roux, C., Alber, A., Bertrand, M., Vaudor, L., Piégay, H., 2015. "FluvialCorridor": a new ArcGIS toolbox package for multiscale riverscape exploration. Geomorphology 242, 29–37. https://doi.org/10.1016/j.geomorph.2014.04.018.
Ruiz-Villanueva, V., Badoux, A., Rickenmann, D., Böckli, M., Schläfli, S., Steeb, N., Stoffel, M., Rickli, C., 2018. Impacts of a large flood along a mountain river basin: the importance of channel widening and estimating the large wood budget in the upper emme river (Switzerland). Earth Surf. Dynam. 6, 1115–1137. https://doi.org/10.5194/esurf-6-1115-2018.
Ruiz-Villanueva, V., Piégay, H., Scorpio, V., Bachmann, A., Brousse, G., Cavalli, M., Comiti, F., Crema, S., Fernández, E., Furdada, G., Hajdukiewicz, H., Hunzinger, L., Lucía, A., Marchi, L., Moraru, A., Piton, G., Rickenmann, D., Righini, M., Surian, N., Yassine, R., Wyżga, B., 2023. River widening in mountain and foothill areas during floods: insights from a meta-analysis of 51 european rivers. Sci. Total Environ. 903, 166103. https://doi.org/10.1016/j.scitotenv.2023.166103.
Sanchez, G., Rolland, Y., Schneider, J., Corsini, M., Oliot, E., Goncalves, P., Verati, C., Lardeaux, J.-M., Marquer, D., 2011. Dating low-temperature deformation by 40Ar/39Ar on white mica, insights from the Argentera-Mercantour massif (SW alps). Lithos 125, 521–536. https://doi.org/10.1016/j.lithos.2011.03.009.
Scorpio, V., Crema, S., Marra, F., Righini, M., Ciccarese, G., Borga, M., Cavalli, M., Corsini, A., Marchi, L., Surian, N., Comiti, F., 2018. Basin-scale analysis of the geomorphic effectiveness of flash floods: a study in the northern apennines (Italy). Sci. Total Environ. 640–641, 337–351. https://doi.org/10.1016/j.scitotenv.2018.05.252.
Scorpio, V., Cavalli, M., Steger, S., Crema, S., Marra, F., Zaramella, M., Borga, M., Marchi, L., Comiti, F., 2022. Storm characteristics dictate sediment dynamics and geomorphic changes in mountain channels: a case study in the italian alps. Geomorphology 403, 108173. https://doi.org/10.1016/j.geomorph.2022.108173.
Sholtes, J.S., Yochum, S.E., Scott, J.A., Bledsoe, B.P., 2018. Longitudinal variability of geomorphic response to floods. Earth Surf. Process. Landf. 43, 3099–3113. https://doi.org/10.1002/esp.4472.
Smith, G.A., 1986. Coarse-grained nonmarine volcaniclastic sediment: terminology and depositional process. Geol. Soc. Am. Bull. 97, 1. https://doi.org/10.1130/0016-7606(1986)97<1:CNVSTA>2.0.CO;2.
Sohn, 1997. On traction-carpet sedimentation. SEPM JSR 67. https://doi.org/10.1306/D42685AE-2B26-11D7-8648000102C1865D.
Steinritz, V., Bellanova, P., Schmidt, B., Schüttrumpf, H., Schwarzbauer, J., Reicherter, K., 2024. Geomorphic changes after the 2021 central european flood in the ahr valley by LiDAR-based differences. Environ. Sci. Eur. 36, 75. https://doi.org/10.1186/s12302-024-00893-x.
Straub, K.M., Duller, R.A., Foreman, B.Z., Hajek, E.A., 2020. Buffered, incomplete, and shredded: the challenges of reading an imperfect stratigraphic record. JGR Earth Surface 125, e2019JF005079. https://doi.org/10.1029/2019JF005079.
Surian, N., Righini, M., Lucía, A., Nardi, L., Amponsah, W., Benvenuti, M., Borga, M., Cavalli, M., Comiti, F., Marchi, L., Rinaldi, M., Viero, A., 2016. Channel response to extreme floods: insights on controlling factors from six mountain rivers in northern apennines, Italy. Geomorphology 272, 78–91. https://doi.org/10.1016/j.geomorph.2016.02.002.
Takahashi, T., 2014. Debris Flow: Mechanics, Prediction, and Countermeasures, 2nd ed. CRC press, Boca Raton.
Thouret, J.-C., Antoine, S., Magill, C., Ollier, C., 2020. Lahars and debris flows: characteristics and impacts. Earth Sci. Rev. 201, 103003. https://doi.org/10.1016/j.earscirev.2019.103003.
Tjalling De Haas, Wilco Van Den Berg, Lisanne Braat, Marteen G. Klein Hans, 2016. Autogenic avulsion, channelization and backfilling dynamics of debris-flow fans. Sedimentology 63, 1596–1619. https://doi.org/10.1111/sed.12275.
Tofelde, S., Bernhardt, A., Guerit, L., Romans, B.W., 2021. Times associated with source-to-sink propagation of environmental signals during landscape transience. Front. Earth Sci. 9, 628315. https://doi.org/10.3389/feart.2021.628315.
Venditti, J.G., Church, M., Bennett, S.J., 2005. On the transition between 2D and 3D dunes. Sedimentology 52, 1343–1359. https://doi.org/10.1111/j.1365-3091.2005.00748.x.
Walling, D.E., Webb, B.W., 1996. Erosion and sediment yield: a global overview. AHS Publications-Series of Proceedings and Reports-Intern Assoc Hydrological Sciences 3–20.
Yochum, S.E., Sholtes, J.S., Scott, J.A., Bledsoe, B.P., 2017. Stream power framework for predicting geomorphic change: the 2013 Colorado front range flood. Geomorphology 292, 178–192. https://doi.org/10.1016/j.geomorph.2017.03.004.